JLAB-THY-99-36

Photo- and Electro-Disintegration of ^{3}He at Threshold and *pd* Radiative Capture

M. Viviani

INFN, Sezione di Pisa, I-56100 Pisa, Italy

A. Kievsky

INFN, Sezione di Pisa, I-56100 Pisa, Italy

L. E. Marcucci

Department of Physics, Old Dominion University, Norfolk, Virginia 23529

S. Rosati

Department of Physics, University of Pisa, I-56100 Pisa, Italy

and

INFN, Sezione di Pisa, I-56100 Pisa, Italy

R. Schiavilla

Jefferson Lab, Newport News, Virginia 23606

and

Department of Physics, Old Dominion University, Norfolk, Virginia 23529

(April 4, 2000)

arXiv:nucl-th/9911051 15 Nov 1999

Abstract

The present work reports results for: i) *pd* radiative capture observables measured at center-of-mass (c.m.) energies in the range 0–100 keV and at 2 MeV by the TUNL and Wisconsin groups, respectively; ii) contributions to the Gerasimov-Drell-Hearn (GDH) integral in ^{3}He from the two- up to the three-body breakup thresholds, compared to experimental determinations by the TUNL group in this threshold region; iii) longitudinal, transverse, and interference response functions measured in inclusive polarized electron scattering off polarized ^{3}He at excitation energies below the threshold for breakup into *ppn*, compared to unpolarized longitudinal and transverse data from the Saskatoon group. The calculations are based on pair-correlated-hyperspherical-harmonics bound and continuum wave functions obtained from a realistic Hamiltonian consisting of the Argonne v_{18} two-nucleon and Urbana IX three-nucleon interactions. The electromagnetic current operator includes one- and two-body components, leading terms of which are constructed from the Argonne v_{18} interaction (specifically, its charge-independent part). Two-body currents associated with Δ-isobar degrees of freedom are treated non-perturbatively via the transition-correlation-operator method. The theoretical predictions obtained by including only one-body currents are in violent disagreement with data. These differences between theory and experiment are, to a large extent, removed when two-body currents are taken into account, although some rather large discrepancies remain in the c.m. energy range 0–100 keV, particularly for the *pd* differential cross section $\sigma(\theta)$ and tensor analyzing power $T_{20}(\theta)$ at small angles, and contributions to the GDH integral. A rather detailed analysis indicates that these discrepancies have, in large part, a common origin, and can be traced back to an excess strength obtained in the theoretical calculation of the E_1 reduced matrix element associated with the *pd* channel having $L, S, J = 1, 1/2, 3/2$. It is suggested that this lack of E_1 strength observed experimentally might have implications for the nuclear interaction at very low energies. Finally, the validity of the long-wavelength approximation for electric dipole transitions is discussed.

21.45.+v, 24.70.+s, 25.30.Fj, 25.40.Lw, 27.10.+h

Typeset using REVTeX

I. INTRODUCTION

Radiative capture, photo- and electro-disintegration reactions are a useful tool for exploring the structure of nuclei and their electromagnetic response. The theoretical description of these processes requires knowledge of the nuclear bound- and scattering-state wave functions and electromagnetic transition operators. In this respect, the trinucleon systems play a unique role because of the capability, achieved in the last few years, to obtain very accurate wave functions for both bound and continuum states from realistic Hamiltonian models [1–4].

The accuracy of the calculated trinucleon continuum wave functions has been verified by comparing results for a variety of Nd scattering observables obtained by a number of groups using different techniques (see Ref. [1] and references therein). In fact, good overall agreement exists between theory and experiment for both elastic and inelastic Nd cross sections and polarization observables, with the only notable exceptions of the *pd* and *nd* vector analyzing powers at low energies, which are both underpredicted by theory at the 30% level [1,5]. Indeed, the A_y "puzzle" constitutes an excellent example of how, once the numerical uncertainties in the calculation of the continuum wave functions have been drastically reduced, Nd scattering observables can be used to study the sentitivity to two- and three-nucleon interaction models.

Electromagnetic processes, such as the low-energy *pd* radiative fusion and threshold photo- and electro-disintegration of ^{3}He under consideration in the present work, provide additional and essential insights into the structure of the trinucleons, since they can be used to test and refine (or possibly, discriminate among) models for the nuclear interactions and electromagnetic transition operators. Furthermore, they allow us to study a number of other, closely related issues. A specific example of these is the relevance of Δ-isobar degrees of freedom for the proper description of photo- and electro-nuclear observables [6].

There are now available many high-quality data, including differential cross sections, vector and tensor analyzing powers, and photon polarization coefficients, on the *pd* radiative capture at c.m. energies ranging from 0 to 2 MeV [7–9]. The goal of the present study is to determine the extent to which this rich body of data can be described satisfactorily by a calculation based on a realistic Hamiltonian (consisting of the Argonne v_{18} two-nucleon [10] and Urbana-IX three-nucleon [11] interactions), and a current operator including one- and two-body components, leading terms of which are constructed consistently with the two-nucleon interaction. The present work updates and extends previous ones, which only dealt with *pd* radiative capture in the c.m. energy range 0–100 keV and *nd* radiative capture at thermal neutron energies [6]. It contains: i) an improved treatment of the *pd* continuum within the pair-correlated-hyperspherical-harmonics (PHH) scheme; ii) calculations of *pd* radiative capture polarization observables in the c.m. energy range 0–100 keV, measured by the TUNL group [7], and at 2 MeV, measured by the Wisconsin group [9]; iii) a calculation of the contribution to the Gerasimov-Drell-Hearn integral of ^{3}He in the threshold region, compared to results of an experimental determination by the TUNL group [12]; and iv) a calculation of the longitudinal, transverse, and interference response functions measured in inclusive scattering of polarized electrons off polarized ^{3}He for excitation energies below the three-body breakup threshold and for momentum transfers up to 5 fm^{-1}, compared with longitudinal and transverse data measured by Retzlaff *et al.* [13] at q=0.88, 1.54 and 2.47 fm^{-1}.

The paper is organized into five sections and an appendix. In Sec. II we discuss the calculation of the bound and scattering wave functions with the PHH method, and summarize a number of results obtained for *Nd* elastic scattering observables, comparing them to experimental data. In Sec. III we briefly review the model for the electromagnetic transition operator, while in Sec. IV we present an exhaustive comparison between theory and experiment for all available *pd* capture, photo- and electro-disintegration data in the threshold region. Finally, in Sec. V we summarize our conclusions. A collection of formulas for the calculation of various observables from the reduced matrix elements of the current and charge operators, which complement those published earlier in Ref. [6], are given in the Appendix.

II. BOUND- AND SCATTERING-STATE WAVE FUNCTIONS

The ^{3}He bound-state and *pd* scattering-state wave functions are obtained variationally with the pair-correlated-hyperspherical-harmonics (PHH) method from a realistic Hamiltonian including the Argonne v_{18} two-nucleon [10] and Urbana-IX three-nucleon [11] interactions (the AV18/UIX model). The PHH method, as implemented in the calculations reported in the present work, has been developed by Kievsky, Rosati and Viviani in a series of papers appeared in various journals between 1993 and 1995 [2,3,14]. Here it will be reviewed briefly for completeness, and a summary of relevant results obtained with it for the three-nucleon bound-state properties and Nd scattering observables at energies below the three-body breakup thresholds will be presented.

The three-nucleon bound-state wave function Ψ_3 is expanded as [14]

$$\Psi_3 = \sum_{\alpha,K} \frac{u_{\alpha K}(\rho)}{\rho^{5/2}} \sum_{\text{cyclic}\, ijk} Z_{\alpha K}(i;jk) \ , \tag{2.1}$$

where ρ is the hyperradius, $\rho = \sqrt{x_i^2 + y_i^2}$ with the Jacobi variables $\mathbf{x}_i$ and $\mathbf{y}_i$ defined, respectively, as $\mathbf{x}_i = \mathbf{r}_j - \mathbf{r}_k$ and $\mathbf{y}_i = (\mathbf{r}_j + \mathbf{r}_k - 2\,\mathbf{r}_i)/\sqrt{3}$. The known functions $Z_{\alpha K}(i;jk)$ are antisymmetric under the exchange $j \rightleftharpoons k$ and account for the angle-spin-isospin and hyperangle dependence of channel α, K. The index α denotes collectively the spectator i and pair jk orbital and spin angular momenta and isospins coupled to produce a state with total angular momentum and isospin $J^\pi, T = \frac{1}{2}^+, \frac{1}{2}$, while the index K specifies the order of the Jacobi polynomial in the hyperangle $\cos\phi_i = x_i/\rho$. Correlation factors, which account for the strong state-dependent correlations induced by the nucleon-nucleon interaction, are included in the functions $Z_{\alpha K}(i;jk)$.

The Rayleigh-Ritz variational principle,

$$\langle \delta_u \Psi_3 | H - E_3 | \Psi_3 \rangle = 0 \ \ , \tag{2.2}$$

is used to determine the functions $u_{\alpha K}(\rho)$. Carrying out the variations with respect to the $u_{\alpha K}$'s leads to a set of coupled second-order differential equations. After discretization in the variable ρ, this set of differential equations is converted into a generalized eigenvalue problem, which is then solved by standard numerical techniques [14].

Fully converged AV18/UIX PHH wave functions predict three-nucleon binding energies and matter radii respectively given by $B(^3\text{H})$ =8.48 MeV and $\langle r^2(^3\text{H})\rangle^{1/2} = 1.725$ fm, $B(^3\text{He}) = 7.73$ MeV and $\langle r^2(^3\text{He})\rangle^{1/2} = 1.928$ fm, in agreement with corresponding "exact" Green's function Monte Carlo results [4] and with the available experimental data.

The Nd cluster wave function $\Psi_{1+2}^{LSJJ_z}$, having incoming orbital angular momentum L and channel spin S ($S = 1/2, 3/2$) coupled to total JJ_z, is expressed as

$$\Psi_{1+2}^{LSJJ_z} = \Psi_C^{JJ_z} + \Psi_A^{LSJJ_z} \ , \tag{2.3}$$

where Ψ_C vanishes in the limit of large intercluster separation, and hence describes the system in the region where the particles are close to each other and their mutual interactions are large. In the asymptotic region, where intercluster interactions are negligible, $\Psi_A^{LSJJ_z}$ (for pd, as an example) is written as

$$\Psi_A^{LSJJ_z} = \sum_{\text{cyclic}\, ijk} \sum_{L'S'} \Big[[s_i \otimes \phi_d(\mathbf{x}_i)]_{S'} \otimes Y_{L'}(\hat{\mathbf{y}}_i) \Big]_{JJ_z} \times \left[\delta_{LL'}\delta_{SS'} \frac{F_{L'}(pr_{pd})}{pr_{pd}} + R^J_{LS,L'S'}(p) \frac{G_{L'}(pr_{pd})}{pr_{pd}} g(r_{pd}) \right] \ , \tag{2.4}$$

where ϕ_d is the deuteron wave function, p the magnitude of the relative momentum between deuteron and proton, and F_L and G_L are the regular and irregular Coulomb functions, respectively. Note that for nd scattering, $F_L(x)/x$ and $G_L(x)/x$ are to be replaced by the regular and irregular spherical Bessel functions. The function $g(r_{pd})$ modifies the $G_L(pr_{pd})$ at small r_{pd} by regularizing it at the origin, and $g(r_{pd}) \rightarrow 1$ as $r_{pd} \geq 10$ fm, thus not affecting the asymptotic behavior of $\Psi_{1+2}^{LSJJ_z}$. Finally, the real parameters $R^J_{LS,L'S'}(p)$ are the R-matrix elements which determine phase-shifts and (for coupled channels) mixing angles at the energy $p^2/(2\mu)$, μ being the 1+2 reduced mass. Of course, the sum over $L'S'$ is over all values compatible with a given J and parity.

The "core" wave function Ψ_C is expanded in the same PHH basis as the bound-state wave function Ψ_3, Eq. (2.1), and both the matrix elements $R^J_{LS,L'S'}(p)$ and functions $u_{\alpha K}(\rho)$

occurring in the expansion of Ψ_C are determined by making the functional [2,3]

$$[R^J_{LS,L'S'}(p)] = R^J_{LS,L'S'}(p) - \langle \Psi^{L'S'JJ_z}_{1+2} | H - E_2 - \frac{p^2}{2\mu} | \Psi^{LSJJ_z}_{1+2} \rangle \ , \tag{2.5}$$

stationary with respect to variations in the $R^J_{LS,L'S'}$ and $u_{\alpha K}$ (Kohn variational principle). Here $E_2 = -2.225$ MeV is the deuteron energy.

Phase-shifts and mixing angles for *nd* scattering at energies below the three-body breakup threshold have been obtained from a realistic Hamiltonian model, and have been shown to be in excellent agreement with corresponding Faddeev results [15], thus establishing the high accuracy of the PHH expansion for the scattering problem. It is important to emphasize that the PHH scheme, in contrast to momentum-space Faddeev methods, permits the straightforward inclusion of Coulomb distortion effects in the *pd* channel. The PHH results for *pd* elastic scattering are as accurate as those for *nd* scattering.

The *nd* and *pd* doublet and quartet scattering lengths predicted by the AV18/UIX model are listed in Table I, and are found to be in excellent agreement with the available experimental values.

III. THE ELECTROMAGNETIC CURRENT OPERATOR

The nuclear charge and current operators consist of one- and two-body terms that operate on the nucleon degrees of freedom:

$$\rho(\mathbf{q}) = \sum_i \rho^{(1)}_i(\mathbf{q}) + \sum_{i<j} \rho^{(2)}_{ij}(\mathbf{q}) \ , \tag{3.1}$$

$$\mathbf{j}(\mathbf{q}) = \sum_i \mathbf{j}^{(1)}_i(\mathbf{q}) + \sum_{i<j} \mathbf{j}^{(2)}_{ij}(\mathbf{q}) \ , \tag{3.2}$$

where $\mathbf{q}$ is the momentum transfer.

The one-body operators $\rho^{(1)}_i$ and $\mathbf{j}^{(1)}_i$ have the standard expressions obtained from a relativistic reduction of the covariant single-nucleon current, and are listed below for convenience. The charge operator is written as

$$\rho^{(1)}_i(\mathbf{q}) = \rho^{(1)}_{i,\mathrm{NR}}(\mathbf{q}) + \rho^{(1)}_{i,\mathrm{RC}}(\mathbf{q}) \ , \tag{3.3}$$

with

$$\rho^{(1)}_{i,\mathrm{NR}}(\mathbf{q}) = \epsilon_i \, \mathrm{e}^{\mathrm{i}\mathbf{q}\cdot\mathbf{r}_i} \ , \tag{3.4}$$

$$\rho^{(1)}_{i,\mathrm{RC}}(\mathbf{q}) = \left(\frac{1}{\sqrt{1+q_\mu^2/4m^2}} - 1 \right) \epsilon_i \, \mathrm{e}^{\mathrm{i}\mathbf{q}\cdot\mathbf{r}_i} - \frac{\mathrm{i}}{4m^2} \left(2\,\mu_i - \epsilon_i\right) \mathbf{q} \cdot (\boldsymbol{\sigma}_i \times \mathbf{p}_i) \, \mathrm{e}^{\mathrm{i}\mathbf{q}\cdot\mathbf{r}_i} \ , \tag{3.5}$$

where $q_\mu^2 = q^2 - \omega^2$ is the four-momentum transfer, and ω is the energy transfer. The current operator is expressed as

$$\mathbf{j}^{(1)}_i(\mathbf{q}) = \frac{1}{2m} \epsilon_i \left[\mathbf{p}_i \, , \, \mathrm{e}^{\mathrm{i}\mathbf{q}\cdot\mathbf{r}_i} \right]_+ - \frac{\mathrm{i}}{2m} \mu_i \, \mathbf{q} \times \boldsymbol{\sigma}_i \, \mathrm{e}^{\mathrm{i}\mathbf{q}\cdot\mathbf{r}_i} \ , \tag{3.6}$$

where $[\cdots \, , \, \cdots]_+$ denotes the anticommutator. The following definitions have been introduced:

$$\epsilon_i \equiv \frac{1}{2} \left[G_E^S(q_\mu^2) + G_E^V(q_\mu^2) \tau_{z,i} \right] \ , \tag{3.7}$$

$$\mu_i \equiv \frac{1}{2} \left[G_M^S(q_\mu^2) + G_M^V(q_\mu^2) \tau_{z,i} \right] \ , \tag{3.8}$$

and $\mathbf{p}$, $\boldsymbol{\sigma}$, and $\boldsymbol{\tau}$ are the nucleon's momentum, Pauli spin and isospin operators, respectively. The two terms proportional to $1/m^2$ in $\rho^{(1)}_{i,\mathrm{RC}}$ are the well known Darwin-Foldy and spin-orbit relativistic corrections [16,17], respectively.

The dipole parametrization is used for the isoscalar (S) and isovector (V) combinations of the electric and magnetic nucleon form factors (including the Galster form for the electric neutron form factor [18]). It is worth emphasizing that the neutron form factors, particularly the electric one, are not well known and, therefore, the available semi-empirical parameterizations for them differ widely, particularly at high momentum transfers. Until this uncertainty in the detailed behavior of the electromagnetic form factors of the nucleon is narrowed, quantitative predictions of electronuclear observables at high momentum transfers will remain somewhat tentative.

The most important features of the two-body parts of the electromagnetic current operator are summarized below. The reader is referred to Refs. [6,19] for a derivation and listing of their explicit expressions.

A. Two-body current operators

The two-body current operator has "model-independent"and "model-dependent "components, in the classification scheme of Riska [20]. The model-independent terms are obtained from the charge-independent part of the AV18, and by construction [21] satisfy current conservation with this interaction. The leading operator is the isovector "π-like "current obtained from the isospin-dependent spin-spin and tensor interactions. The latter also generate an isovector "ρ-like "current, while additional model-independent isoscalar and isovector currents arise from the isospin-independent and isospin-dependent central and momentum-dependent interactions. These currents are short-ranged and numerically far less important than the π-like current.

The model-dependent currents are purely transverse and therefore cannot be directly linked to the underlying two-nucleon interaction. The present calculation includes the isoscalar $\rho\pi\gamma$ and isovector $\omega\pi\gamma$ transition currents as well as the isovector current associated with excitation of intermediate Δ-isobar resonances. The $\rho\pi\gamma$ and $\omega\pi\gamma$ couplings are known from the measured widths of the radiative decays $\rho \rightarrow \pi\gamma$ [22] and $\omega \rightarrow \pi\gamma$ [23], respectively, while their momentum-transfer dependence is modeled using vector-meson-dominance. Monopole form factors are introduced at the meson-baryon vertices with cutoff values of Λ_π=3.8 fm^{-1} and Λ_ρ=Λ_ω=6.3 fm^{-1} at the πNN, ρNN and ωNN vertices, respectively.

Among the model-dependent currents, those associated with the Δ-isobar are the most important ones. In the present calculation, these currents are treated within the transition-correlation-operator (TCO) scheme developed in Ref. [24]. In such an approach, the Δ degrees of freedom are explicitly included in the nuclear wave functions by writing

$$\Psi_{N+\Delta} = \left[\mathcal{S} \prod_{i<j} \left(1 + U_{ij}^{TR} \right) \right] \Psi \ , \tag{3.9}$$

where Ψ is the purely nucleonic component, $\mathcal{S}$ is the symmetrizer and the transition correlations U_{ij}^{TR} are short-range operators, that convert NN pairs into $N\Delta$ and $\Delta\Delta$ pairs.

In the present study the Ψ is taken from PHH solutions of the AV18/UIX Hamiltonian with nucleons only interactions, while the U_{ij}^{TR} is obtained from two-body bound and low-energy scattering state solutions of the full N-Δ coupled-channel problem. This aspect of the present calculations as well as the justification for going beyond the traditional perturbative treatment of Δ degrees of freedom in nuclei, were discussed at length in the original work [24], and have been reviewed most recently in Ref. [25], making a further review here unnecessary.

In the TCO approach, both $\gamma N\Delta$ and $\gamma\Delta\Delta$ M_1 couplings are considered [24]. The values used for these couplings are, respectively, $\mu_{\gamma N\Delta} = 3$ n.m. and $\mu_{\gamma\Delta\Delta} = 4.35$ n.m. The former is taken from an analysis of γN data in the Δ-resonance region [26], while the latter is obtained from a soft-photon analysis of pion-proton bremsstrahlung data near the Δ^{++} resonance [27].

Electromagnetic observables require evaluation of matrix elements of the type [24,25]

$$\frac{\langle \Psi_{N+\Delta,f} \,|\, \mathbf{j} \,|\, \Psi_{N+\Delta,i} \rangle}{[\langle \Psi_{N+\Delta,f} \,|\, \Psi_{N+\Delta,f} \rangle \langle \Psi_{N+\Delta,i} \,|\, \Psi_{N+\Delta,i} \rangle]^{1/2}} \ , \tag{3.10}$$

where the wave functions and currents include both nucleonic and Δ-isobar degrees of freedom. To evaluate such a matrix element, it is convenient to expand the wave function $\Psi_{N+\Delta}$ as

$$\Psi_{N+\Delta} = \Psi + \sum_{i<j} U_{ij}^{TR} \Psi + \dots \ , \tag{3.11}$$

and write the numerator of Eq. (3.10), in a schematic notation, as

$$\langle \Psi_{N+\Delta,f} \,|\, \mathbf{j} \,|\, \Psi_{N+\Delta,i} \rangle \ = \ \langle \Psi_f \,|\, \mathbf{j}(N\,\mathrm{only}) \,|\, \Psi_i \rangle \ + \ \langle \Psi_f \,|\, \mathbf{j}(\Delta) \,|\, \Psi_i \rangle \ , \tag{3.12}$$

where $\mathbf{j}(N\,\mathrm{only})$ denotes all one- and two-body contributions to $\mathbf{j}(\mathbf{q})$ which only involve nucleon degrees of freedom, i.e., $\mathbf{j}(N\,\mathrm{only}) \ = \ \mathbf{j}^{(1)}(N \rightarrow N) \ + \ \mathbf{j}^{(2)}(NN \rightarrow NN)$. The operator $\mathbf{j}(\Delta)$ includes terms involving the Δ-isobar degrees of freedom, associated with the explicit Δ currents $\mathbf{j}^{(1)}(N \rightarrow \Delta)$, $\mathbf{j}^{(1)}(\Delta \rightarrow N)$, and $\mathbf{j}^{(1)}(\Delta \rightarrow \Delta)$, and with the transition operators U_{ij}^{TR}. Of course, the presence of Δ admixtures in the wave functions also influences their normalization.

Finally, we note that the contributions associated with the $\rho\pi\gamma$, $\omega\pi\gamma$ and Δ-excitation mechanisms are, at low and moderate values of momentum transfer ($q \leq 5$ fm^{-1}), typically much smaller than those due to the leading model-independent π-like current [6,25].

B. Two-body charge operators

While the main parts of the two-body currents are linked to the form of the two-nucleon interaction through the continuity equation, the most important two-body charge operators are model-dependent, and should be considered as relativistic corrections. Indeed, a consistent calculation of two-body charge effects in nuclei would require the inclusion of relativistic effects in both the interaction models and nuclear wave functions. Such a program is just at its inception for systems with $A \geq 3$. There are nevertheless rather clear indications for the relevance of two-body charge operators from the failure of the impulse approximation (IA) in predicting the deuteron tensor polarization observable [28], and charge form factors of the three- and four-nucleon systems [19,25]. The model commonly used [29] includes the π-, ρ-, and ω-meson exchange charge operators with both isoscalar and isovector components, as well as the (isoscalar) $\rho\pi\gamma$ and (isovector) $\omega\pi\gamma$ charge transition couplings, in addition to the single-nucleon Darwin-Foldy and spin-orbit relativistic corrections. The π- and ρ-meson exchange charge operators are constructed from the AV18 isospin-dependent spin-spin and tensor interactions, using the same prescription adopted for the corresponding current operators. It should be emphasized, however, that for $q < 5$ fm^{-1} the contribution due to the π-exchange charge operator is typically an order of magnitude larger than that of any of the remaining two-body mechanisms and one-body relativistic corrections.

IV. RESULTS

The present section contains results for the *pd* radiative capture in the c.m. energy range 0–100 keV, compared to the TUNL data [7,8], and at 2 MeV, compared to the Wisconsin data [9], as well as results for the threshold electrodisintegration of ^{3}He at momentum transfers q=0.88, 1.64 and 2.74 fm^{-1}, compared to Bates data [13]. It also contains predictions for the contribution to the Gerasimov-Drell-Hearn integral of ^{3}He up to the three-body breakup threshold, compared to a very recent experimental determination of this contribution in the *pd* threshold region by the TUNL group [12].

The calculations are based on bound- and scattering-state PHH wave functions, obtained from the Argonne v_{18} two-nucleon and Urbana-IX three-nucleon interactions (see discussion in Sec. II). The model for the electromagnetic current operator includes one- and two-body components, leading terms of which are constructed from the two-nucleon interaction (in the present case, the charge independent part of the AV18). The currents associated with the excitation of Δ-isobars are treated non-perturbatively within the transition-correlation-operator scheme, as sketched in Sec. III.

A study of the *pd* capture cross section and polarization observables in the c.m. energy range 0–100 keV was reported earlier in Ref. [6]. In the present work, improvements in the PHH variational treatment of the P-wave *pd* channel have led to significant changes in the predictions for the S-factor and some of the polarization observables, particularly the vector analyzing power A_y, than previously published [6]. We therefore provide an update of that study.

A. The *pd* capture below 100 keV c.m. energy

The observed linear dependence upon the energy of the S-factor and the observed angular distributions of the polarization observables indicate that the *pd* radiative fusion proceeds, at these low energies, through S- and P-wave captures. Therefore, the contributing reduced matrix elements (RMEs) are $M_1^{0\frac{1}{2}\frac{1}{2}}$, $M_1^{0\frac{3}{2}\frac{3}{2}}$, and $E_2^{0\frac{3}{2}\frac{3}{2}}$ in S-wave capture, and $E_1^{1\frac{1}{2}\frac{1}{2}}$, $E_1^{1\frac{1}{2}\frac{3}{2}}$, $E_1^{1\frac{3}{2}\frac{1}{2}}$, $E_1^{1\frac{3}{2}\frac{3}{2}}$, $M_2^{1\frac{1}{2}\frac{3}{2}}$, and $M_2^{1\frac{3}{2}\frac{3}{2}}$ in P-wave capture, where M_ℓ and E_ℓ are the magnetic and electric ℓth–pole operators, respectively. The superscripts LSJ refer to the relative orbital angular momentum L between the p and d clusters, the channel spin S (S = 1/2 or 3/2), and the total angular momentum J ($\mathbf{J} = \mathbf{L} + \mathbf{S}$), respectively. The M_2 transition from the L, S, J =1,3/2,5/2 capture state has been neglected.

Improvements in the PHH description of the *pd* continuum wave functions, particularly in the short-range part, have led to significative changes in the values of the P-wave capture RMEs than previously calculated [6]. The S-wave capture RME values have remained essentially unchanged.

The E_1 RMEs have in fact been calculated in two different ways: firstly, by direct evaluation of the matrix elements of the E_1 multipole operator,

$$E_1^{LSJ} = \frac{\sqrt{2}}{\langle JJ_z, 1\lambda | \frac{1}{2}\sigma_3 \rangle} \langle \Psi_3^{\frac{1}{2}\sigma_3} | E_{1\lambda} | \overline{\Psi}_{1+2}^{LSJJ_z} \rangle \ , \tag{4.1}$$

$$E_{1\lambda} = \frac{1}{q} \int d\mathbf{x}\, \mathbf{j}(\mathbf{x}) \cdot \nabla \times j_1(qx) \mathbf{Y}_{1\lambda}^{11}(\hat{\mathbf{x}}) \ , \tag{4.2}$$

where $\mathbf{j}(\mathbf{x})$ is the nuclear current density operator, $j_1(qx)$ is the spherical Bessel function of order one, $\mathbf{Y}_{1\lambda}^{11}(\hat{\mathbf{x}})$ are vector spherical harmonic functions, and the *pd* wave function is constructed to satisfy outgoing-wave boundary conditions as in Eq. (4.3) of Ref. [6].

Secondly, in the long-wavelength-approximation (LWA) (certainly justified in the energy range under consideration here) the E_1 operator can be expressed as [30]

$$E_{1\lambda} \simeq E_{1\lambda}(\text{LWA1}) + E_{1\lambda}(\text{LWA2}) + E_{1\lambda}(\text{LWA3}) \ , \tag{4.3}$$

where

$$E_{1\lambda}(\text{LWA1}) = -\frac{\sqrt{2}}{3} \left[H\, , \int d\mathbf{x}\, x\, Y_{1\lambda}(\hat{\mathbf{x}})\, \rho(\mathbf{x}) \right] \ , \tag{4.4}$$

$$E_{1\lambda}(\text{LWA2}) = \frac{\mathrm{i}\, q^2}{3\sqrt{2}} \int d\mathbf{x}\, x\, Y_{1\lambda}(\hat{\mathbf{x}})\, \mathbf{x} \cdot \mathbf{j}(\mathbf{x}) \ , \tag{4.5}$$

$$E_{1\lambda}(\text{LWA3}) = \frac{\sqrt{2}\, q^2}{15} \left[H\, , \int d\mathbf{x}\, x^3\, Y_{1\lambda}(\hat{\mathbf{x}})\, \rho(\mathbf{x}) \right] \ . \tag{4.6}$$

Here the continuity equation has been used to relate $\nabla \cdot \mathbf{j}(\mathbf{x})$ occurring in $E_{1\lambda}$(LWA1) and $E_{1\lambda}$(LWA3) to the commutator $-\mathrm{i}[H\, , \rho(\mathbf{x})]$, where $\rho(\mathbf{x})$ is the charge density operator. Evaluating the RMEs of these operators leads to

$$E_1^{LSJ} \simeq E_1^{LSJ}(\text{LWA1}) + E_1^{LSJ}(\text{LWA2}) \ , \tag{4.7}$$

with

$$E_1^{LSJ}(\text{LWA1}) = \frac{\sqrt{2}}{\langle JJ_z, 1\lambda|\frac{1}{2}\sigma_3\rangle}\frac{\sqrt{2}\,q}{3}\langle\Psi_3^{\frac{1}{2}\sigma_3}|\int d\mathbf{x}\, xY_{1\lambda}(\hat{\mathbf{x}})\rho(\mathbf{x})|\overline{\Psi}_{1+2}^{LSJJ_z}\rangle \ , \tag{4.8}$$

$$E_1^{LSJ}(\text{LWA2}) = \frac{\sqrt{2}}{\langle JJ_z, 1\lambda|\frac{1}{2}\sigma_3\rangle}\frac{\mathrm{i}\,q^2}{3\sqrt{2}}\langle\Psi_3^{\frac{1}{2}\sigma_3}|\int d\mathbf{x}\, xY_{1\lambda}(\hat{\mathbf{x}})\mathbf{x}\cdot\mathbf{j}(\mathbf{x})|\overline{\Psi}_{1+2}^{LSJJ_z}\rangle \ , \tag{4.9}$$

where only terms up to order q^2 have been retained, and it has been assumed that the initial and final PHH wave functions are exact eigenfunctions of the Hamiltonian, so that $[H\, ,\, \rho(\mathbf{x})] \rightarrow -q\,\rho(\mathbf{x})$ in the matrix element. The contribution to the E_1 RMEs associated with the LWA3 operator, defined in Eq. (4.6), is of order q^3, proviso the assumption above.

By ignoring two-body contributions to the charge density operator, we further approximate $\rho(\mathbf{x}) \simeq \rho^{(1)}_{\rm NR}(\mathbf{x}) + \rho^{(1)}_{\rm RC}(\mathbf{x})$, and write correspondingly

$$E_1^{LSJ}(\text{LWA1}) \simeq E_1^{LSJ}(\text{LWAc}) + E_1^{LSJ}(\text{LWAb}) \ , \tag{4.10}$$

where

$$E_1^{LSJ}(\text{LWAc}) = \frac{\sqrt{2}}{\langle JJ_z, 1\lambda|\frac{1}{2}\sigma_3\rangle}\frac{\sqrt{2}\,q}{3}\langle\Psi_3^{\frac{1}{2}\sigma_3}|\sum_i \epsilon_i\, r'_{i,\lambda}|\overline{\Psi}_{1+2}^{LSJJ_z}\rangle \ , \tag{4.11}$$

$$E_1^{LSJ}(\text{LWAb}) = \frac{\sqrt{2}}{\langle JJ_z\, 1\lambda|\frac{1}{2}\sigma_3\rangle}\frac{\sqrt{2}\,q}{3}\langle\Psi_3^{\frac{1}{2}\sigma_3}|\sum_i -\frac{2\mu_i - \epsilon_i}{4m^2}(\boldsymbol{\sigma}_i \times \mathbf{p}_i)_\lambda|\overline{\Psi}_{1+2}^{LSJJ_z}\rangle \ . \tag{4.12}$$

Hence, up to order q^2, the E_1 RMEs in LWA are given by Eq. (4.7), with $E_1^{LSJ}(\text{LWA1})$ defined in Eqs. (4.10)–(4.12). We re-emphasize that the currents used in the present work satisfy, by construction, the continuity equation with the AV18 interaction, namely $\mathbf{q}\cdot\mathbf{j}(\mathbf{q}) = \left[T + v_{18}\, ,\, \rho^{(1)}_{\rm NR}(\mathbf{q})\right]$. Therefore, if the contributions $E_1^{LSJ}(\text{LWAb})$ and $E_1^{LSJ}(\text{LWA2})$ (the latter of order q^2) were to be negligible, the degree of agreement between the $E_1(\text{LWAc})$ and full current results, obtained directly from Eq. (4.1), would simply reflect the extent to which the present variational wave functions are truly exact eigenfunctions of the AV18/UIX Hamiltonian. In Table II the results for the E_1 RMEs obtained by direct evaluation of the

E_1 multipole operator matrix elements given in Eq. (4.1) are compared with those obtained in LWA. Note that the E_1^{LSJ}(LWA2) contribution, Eq. (4.5), has been estimated here by using only the spin-part of the IA current operator. Of course, single-nucleon convection as well as two-body currents provide additional corrections to $\mathbf{j}(\mathbf{x})$, but these have been ignored in the evaluation of Eq. (4.9). Finally, note that the RMEs listed in Table II are related to those defined in Eqs. (4.1) and (4.8)–(4.9) via

$$\widetilde{X}_{\ell C}^{LSJ} = \sqrt{\frac{v_{\rm rel}}{2\pi\alpha}\exp(2\pi\alpha/v_{\rm rel})}\,\frac{\sqrt{6\pi}}{q\mu_N}\,\sqrt{4\pi}\,X_\ell^{LSJ}\ , \tag{4.13}$$

where μ_N is the nuclear magneton and $v_{\rm rel}$ is the *pd* relative velocity. The quantities $\widetilde{X}_{\ell C}^{LSJ}$ are easily shown to remain finite in the limit $v_{\rm rel} \to 0$.

As can be seen by inspection of Table II, for the $S = 1/2$ states the values of the LWAc and "full" E_1 RMEs are very close to each other and the remaining small differences between them are presumably due to the approximate calculation of the E_1^{LSJ}(LWA2) contribution carried out here (see above). Therefore, the present PHH wave functions for these P-wave channels are a good approximation to the true eigenfunctions. This is to be contrasted with the results reported in Table VI of Ref. [6], where significant differences remained particularly for the $S = 1/2$ $J = 1/2$ E_1 RME.

The situation is different for the $S = 3/2$ states. Here, as discussed in Ref. [6] and below, due to cancellations among different contributions, the E_1(LWAc) RMEs are rather small and indeed have similar magnitude as the E_1(LWAb) and E_1(LWA2) RMEs. Hence, if the PHH wave functions for these channels also approximate well the true eigenfunctions-and indeed there is no reason to believe that this is not so-, then the differences between the "full"and LWAc values provide a "measure"of the corrections beyond the standard LWAc. Inspection of Table II in fact shows that the leading LWAc form of the E_1 operator is inadequate for these channels. This point will be further elaborated below and in the next subsection.

As a final remark, note that the continuity equation requires the presence of three-body currents associated with the three-nucleon interaction. These currents have been studied in

Ref. [25], where they were found to give a very small contribution to the trinucleon magnetic moments and form factors. It is, therefore, unlikely that three-body current contributions influence significantly the "full"predictions discussed above, as it was speculated in Ref. [6].

The leading RMEs are the doublet and quartet M_1 in S-wave capture and doublet (namely, $S = 1/2$) E_1's with $J = 1/2$ and $3/2$ in P-wave capture. The M_1 and doublet E_1 strengths are comparable. The E_2 RME is more than an order of magnitude smaller than any of the two M_1's, the quartet (namely, $S = 3/2$) E_1's with $J = 1/2$ and $3/2$ are an order of magnitude smaller than the doublet E_1's, and the M_2 strength is negligible. In LWAc the E_1-multipole operator is spin-independent, and transitions from the ^{3}He ground state to the S=3/2 channel *pd*-states are inhibited, since they must proceed through the relatively small D-wave components of the ^{3}He wave function. Hence, the quartet E_1 RMEs are individually small. Such is not the case for the doublet E_1 RMEs, which result from transitions involving the S=1/2 *pd* states and the dominant S-wave component of the ^{3}He ground state.

The effects due to two-body currents and Δ-degrees of freedom are large on the doublet M_1 RME–at $E_p = 40$ keV, they increase it in magnitude by 87%–and significant on the quartet M_1 RME–at $E_p = 40$ keV, they reduce it by 10%. The $E_1^{1\frac{1}{2}\frac{1}{2}}$ and $E_1^{1\frac{1}{2}\frac{3}{2}}$ RMEs are increased by 7% and 10%, respectively, by two-body current contributions (at $E_p = 40$ keV); however, these contributions dominate the quartet $E_1^{1\frac{3}{2}J}$, interfering destructively with the one-body (IA) results, see Table II.

The calculated S-factor is compared with the TUNL data [7,8] in the lab energy range E_p=0–300 keV in Fig. 1. The present results are in better agreement with data for E_p between 40 and 80 keV than previously reported [6]. However, at higher energies the calculation is slightly above the data, in particular for the data point at E_p=160 keV. Below 40 keV theory is again slightly above the data of Ref. [7].

The calculated S-factor value in S-wave capture at zero energy is 0.110 eV-b, in excellent agreement with the corresponding experimental value 0.109 ± 0.010 eV-b [7]. However, the calculated value in P-wave capture is 0.109 eV-b, which substantially overpredicts the experimental value 0.074 ± 0.01 eV-b [7]. This overprediction at zero energy (and below 40 keV) is due to excess strength in the calculated $L, S, J = 1, 1/2, 3/2$ E_1 RME, as discussed below.

The predicted angular distributions of the differential cross section $\sigma(\theta)$, vector and tensor analyzing powers $A_y(\theta)$ and $T_{20}(\theta)$, and photon linear polarization coefficient $P_\gamma(\theta)$ are compared with the TUNL data from Ref. [7] in Fig 2. As in Ref. [6], we have integrated the theoretical results, weighted with the energy dependence of the cross section and target thickness, for the purpose of comparing them with experiment [31]. The $\simeq 10\%$ changes in the E_1 RMEs, due to the use of more accurate PHH wave functions, are responsible for the improved description of the vector analyzing power A_y which was significantly underpredicted by theory in our earlier work [6]. However, the calculated $\sigma(\theta)$ ($T_{20}(\theta)$) is much smaller (larger) than the experimental values at small angles. The small angle discrepancy for T_{20} was also present in Ref. [6], although it was not as pronounced as found here.

Recently, the TUNL group has measured additional polarization observables at E_p=40 keV [12], specifically the tensor analyzing powers iT_{11}, T_{21}, T_{22} and the circular polarization asymmetry coefficient A_γ. All these observables are found to be in satisfactory agreement with the present calculations [12].

The unpolarized cross section $\sigma(\theta)$ and the tensor analyzing power are given by

$$\sigma(\theta) = \sum_{\ell=0} a_\ell P_\ell(\cos\theta) \ , \qquad \sigma(\theta) T_{20}(\theta) = \sum_{\ell=0} c_\ell P_\ell(\cos\theta) \ , \tag{4.14}$$

where the P_ℓ are Legendre polynomials, and the coefficients a_ℓ and c_ℓ can be expressed in terms of the various RMEs [6]. Hereafter, for ease of presentation, we introduce the notation:

$$m_{2J+1} = M_1^{0JJ} \ , \tag{4.15}$$

$$p_{2J+1} = E_1^{1\frac{1}{2}J} \ , \tag{4.16}$$

$$q_{2J+1} = E_1^{1\frac{3}{2}J} \ , \tag{4.17}$$

the energy dependence of these RMEs being understood. The leading coefficients in the expansion of T_{20} are c_0 and c_2, and their expressions are:

$$c_0 = \sigma_1 \left[2\,\Re(p_2 q_2^*) - \sqrt{\frac{1}{2}}|q_2|^2 - \sqrt{\frac{2}{5}}\Re(p_4 q_4^*) + \sqrt{\frac{8}{25}}|q_4|^2 \right] , \tag{4.18}$$

$$c_2 = \sigma_1 \Big[-\Re(m_2 m_4^*) + \sqrt{\frac{1}{8}}|m_4|^2 - \sqrt{\frac{1}{5}}\Re(p_2 q_4^*) + \sqrt{2}\Re(q_2 p_4^*) \\ + \sqrt{\frac{1}{10}}\Re(q_2 q_4^*) + \sqrt{\frac{1}{10}}\Re(p_4 q_4^*) + \sqrt{\frac{1}{8}}|q_4|^2 \Big] , \tag{4.19}$$

where

$$\sigma_1 = \frac{4\pi}{3} \frac{\alpha q}{v_{\rm rel}} . \tag{4.20}$$

Note that the expression for c_0 reported in Eq. (B7) of Ref. [6] contains several misprints (the different expression for σ_1 used in Ref. [6] accounts for the fact that there the Legendre coefficients were given in terms of the RMEs $\widetilde{X}_\ell^{LSJ}$ defined in Eq. (6.3) of that work).

The coefficients c_0 and c_2 are found to be rather sensitive to the q_2 and q_4 RMEs (in particular, c_0 vanishes if both q_2 and q_4 are set to zero). As discussed above, these RMEs result from transitions connecting small components of the wave functions, and are dominated by many-body current contributions (see Table II). It is not clear, at this stage, whether the discrepancies between the measured and calculated T_{20} (particularly pronounced at small angles) are due to deficiencies in the wave functions, or rather the interactions generating the wave functions, and/or the many-body current models.

The expressions for the leading coefficients a_0 and a_2 in the Legendre expansion of $\sigma(\theta)$ are

$$a_0 = \sigma_1 \left[|m_2|^2 + |m_4|^2 + |p_2|^2 + |q_2|^2 + |p_4|^2 + |q_4|^2 \right] , \tag{4.21}$$

$$a_2 = \sigma_1 \left[\sqrt{2}\Re(p_2 p_4^*) - \frac{1}{2}|p_4|^2 - \frac{1}{\sqrt{5}}\Re(q_2 p_4^*) + \frac{2}{5}|q_4|^2 \right] . \tag{4.22}$$

For these coefficients the contributions of the q_2 and q_4 RMEs are completely negligible, and the observed small-angle discrepancy between theory and experiment is due to excess strength in the calculated p_4 RME, see below. In particular, we have verified that in this low-energy regime the differences between the "full" results and the results obtained by using the LWAc values for the p_2, p_4, q_2 and q_4 RMEs are small for all the observables considered in Fig. 2. This is not the case for the *pd* capture at 2 MeV, as discussed in the next subsection.

The extensive body of data measured at TUNL has allowed the determination of the leading M_1 and E_1 RMEs (magnitudes and phases) via fits to the measured observables [12,31]. The results of this fitting procedure [31] are compared with the calculated RMEs in Table III. The RMEs listed in Table III have been further multiplied by the factor

$$\tilde{x}_{2J+1} = \sqrt{\frac{32\pi\alpha q\mu p}{2J+1}} x_{2J+1} \ , \tag{4.23}$$

where μ is the *pd* reduced mass and α is the fine structure constant, in order to match the different definitions used in the present study and by the authors of the fit. Here, x_{2J+1} stands for either m_{2J+1}, p_{2J+1} or q_{2J+1}. Note that the phase of each RME is simply related to the elastic *pd* phase shift δ^{LSJ}, as discussed in Refs. [9,32]. In particular, at these low energies to a very good approximation $\delta^{LSJ} \simeq \sigma_L$, where σ_L is the L-wave Coulomb phase shift. For example, the phase of the calculated doublet p_2 RME at $E_p = 35$ keV is found to be 22.648°, which is to be compared with an elastic *pd* phase shift $\delta^{1\frac{1}{2}\frac{1}{2}}$ of 22.635° (at this energy, $\sigma_1 = 22.625°$). As can be seen from Table III, the most significant differences between theoretical and experimental RMEs are found for $|\tilde{p}_4|$.

The experimental value of the quartet to doublet ratio, $r_{M1} \equiv 2|\tilde{m}_4|^2/|\tilde{m}_2|^2$, for the M_1 strength had been determined to be 0.49 ± 0.04 in Ref. [33] from an analysis of the T_{20} data at 90°. The value obtained from the "experimental "M_1 RMEs listed in Table III is 0.43 ± 0.05. Both of these are in good agreement with the theoretical prediction of 0.475.

It is interesting to analyze the ratio $r_{E1} \equiv |\tilde{p}_4|^2/|\tilde{p}_2|^2$. Theory gives $r_{E1} \simeq 1$, while from the fit it results that $r_{E1} \approx 0.74 \pm 0.04$. As discussed above, the calculation of these RMEs is not influenced by uncertainties in the two-body currents, since their values are entirely given by the LWAc form of the E_1 operator, which has no spin-dependence. It is therefore of interest to examine more closely the origin of the above discrepancy. If the interactions between the p and d clusters are switched off (hence reducing the *pd* scattering wave function $\Psi_{1+2}^{L=1,SJJ_z}$ in Eq. (2.4) to the product of a deuteron wave function times $Y_1(\hat{\mathbf{r}}_{pd})F_1(qr_{pd})$), the relation $r_{E1} \simeq 1$ then simply follows from angular momentum algebra, apart from negligible corrections due to the small P-wave components of the ^{3}He wave function. Deviations of this ratio from one are therefore to be ascribed to differences induced by the interactions in the $L, S, J = 1, 1/2, 1/2$ and $1, 1/2, 3/2$ wave functions. To study these differences, we define the "density functions" $\tilde{p}_{2J+1}(r_{pd})$ with the property

$$\tilde{p}_{2J+1} = \int_0^\infty dr_{pd}\, \tilde{p}_{2J+1}(r_{pd}) \quad . \tag{4.24}$$

In Fig. 3, the functions $\Re[\tilde{p}_2(r_{pd})]$ and $\Re[\tilde{p}_4(r_{pd})]$ are displayed with and without including intercluster interactions. As expected from the analysis above, the two functions $\Re[\tilde{p}_{2J+1}(r_{pd})]$ are indistinguishable when these interactions are ignored. When the latter are included, the functions $\Re[\tilde{p}_{2J+1}(r_{pd})]$ are shown by the thick dashed ($J = 1/2$) and thick solid ($J = 3/2$) lines. Intercluster interactions have a significant effect reducing, however, both integrated values $\tilde{p}_{2J+1}$ by the same amount $\simeq 10\%$, with the result that $\Re[\tilde{p}_2]$ is still $\simeq \Re[\tilde{p}_4]$.

The AV18/UIX interactions produce essentially the same asymptotic behavior in the J=1/2 and J=3/2 doublet P-wave scattering states. This is directly confirmed by a comparison of the calculated nuclear *pd* elastic phase shifts with the AV18/UIX Hamiltonian model in the $^2P_{1/2}$ and $^2P_{3/2}$ channels, as shown for a few incident proton energies in Table IV. The $^2P_{1/2}$ and $^2P_{3/2}$ phase shifts are found to be very close to each other over the whole energy range considered in the table. Note that the AV18/UIX predictions for these phase shifts at $E_p = 3$ MeV are in excellent agreement with the values extracted from the phase-shift analysis (PSA) performed in Ref. [5].

Therefore, the "experimental" value $r_{E1} = 0.74 \pm 0.04$ is at variance with predictions based on the AV18/UIX Hamiltonian model. It should be emphasized that the present study ignores, in the continuum states, the effects arising from electromagnetic interactions beyond the static Coulomb interaction between protons. It is not clear whether the inclusion of these long-range interactions, in particular their spin-orbit component, could explain the observed splitting between the $\tilde{p}_2$ and $\tilde{p}_4$ RMEs. A calculation incorporating them in the continuum is currently underway, and it will be the subject of a forthcoming paper.

Finally, the calculated A_y and T_{20} analyzing powers at $E_{\rm c.m.} = 75$ keV and 100 keV are compared with the data of Ref. [8] in Fig. 4. Note that the theoretical predictions have changed slightly with respect to the earlier results in Ref. [8], due to the improvement in the description of the *pd* P-waves discussed previously. Somewhat better (worse) agreement between theory and experiment is now found for T_{20} (A_y) than previously reported [8]. The large discrepancy at small angles for T_{20} is present also at these energies.

B. The *pd* capture at 2 MeV

Measurements of capture polarization observables at $E_{\rm c.m.} = 2$ MeV have been reported recently by Smith and Knutson [9], who also extracted, by a fitting procedure, values of the contributing RMEs at this energy. To reduce the number of parameters in the fit, they made use of both *pd* elastic scattering and radiative capture data. In fact, as discussed in Ref. [32], the phases of the radiative capture RMEs are fixed by the elastic S-matrix, when no channels other than elastic or radiative capture ones are open. Furthermore, by using the invariance of the nuclear Hamiltonian under parity and time-reversal transformations, it can be shown that the quantities [9]

$$\overline{\mathcal{E}}_\ell^{LSJ} = {\rm e}^{-{\rm i}\delta^{LSJ}} \sum_{L'S'} U^J_{LS,L'S'} \overline{E}_\ell^{L'S'J} \ , \qquad \overline{\mathcal{M}}_\ell^{LSJ} = {\rm e}^{-{\rm i}\delta^{LSJ}} \sum_{L'S'} U^J_{LS,L'S'} \overline{M}_\ell^{L'S'J} \ , \tag{4.25}$$

are real. In the above expression δ^{LSJ} are the eigenphase shifts and $U^J_{LS,L'S'}$ is the mixing matrix, into which the S-matrix describing *pd* elastic scattering can be decomposed (both the eigenphases and mixing matrix elements are real under the deuteron breakup threshold). The RMEs $\overline{X}_\ell^{LSJ}$ ($X = E,\, M$) used in the expression above are related to the RMEs X_ℓ^{LSJ} defined in the present work (see the Appendix) and in Ref. [6] by

$$\overline{X}_\ell^{LSJ} = {\rm i}^{L+\ell}\,(-1)^{L+S-J} 2\,p \sqrt{\frac{q}{v_{\rm rel}}} \frac{X_\ell^{LSJ}}{\sqrt{2J+1}} \ . \tag{4.26}$$

In Ref. [9], the real quantities $\overline{\mathcal{E}}$ and $\overline{\mathcal{M}}$ have been used as free parameters and extracted from the data. The measured observables, though, were not sufficient to univocally select the values of the RMEs and two sets of parameters have been presented [9]. In order to compare directly with the quantities $\overline{\mathcal{E}}$ and $\overline{\mathcal{M}}$, we have transformed our RMEs via Eqs. (4.25) and (4.26), using the eigenphase shifts and mixing matrices predicted by the AV18/UIX model. The RMEs obtained in this way are reported in Table V along with the two sets of "experimental "values. Inspection of the table indicates that significantly better overall agreement exists between "set 1 "and the theoretical RMEs. We will only consider this set in the discussion to follow.

At this energy, the two doublet E_1's are the dominant RMEs. They have similar values, and are in good agreement with those extracted from the fit. Note that $\overline{\mathcal{E}}_1^{1\frac{1}{2}\frac{1}{2}} \simeq \overline{\mathcal{E}}_1^{1\frac{1}{2}\frac{3}{2}}$ corresponds to $|\tilde{p}_2| \simeq |\tilde{p}_4|$, since the mixing induced by the matrix U in Eq. (4.25) is negligible for these RMEs. Therefore, at this energy the relation $|\tilde{p}_2|^2/|\tilde{p}_4|^2 \simeq 1$ is well verified also by the "experimental "RMEs.

The S-wave M_1 RMEs ($\overline{\mathcal{M}}_1^{0\frac{1}{2}\frac{1}{2}}$ and $\overline{\mathcal{M}}_1^{0\frac{3}{2}\frac{3}{2}}$) are quite well reproduced by theory. Instead, significant differences between theory and experiment are found for the D-wave M_1 RMEs–those extracted from the fit are an order of magnitude larger than predicted by theory. It should be emphasized, however, that most of the observables show sensitivity to these RMEs only in the small ($\theta < 30°$) and large ($\theta > 150°$) angle regions. However, using the experimental values for the D-wave M_1 RMEs, rather than the calculated ones, does not produce "theoretical "observables in significantly better agreement with data.

The "experimental "quartet P-wave E_1 RMEs ($\overline{\mathcal{E}}_1^{1\frac{3}{2}\frac{1}{2}}$ and $\overline{\mathcal{E}}_1^{1\frac{3}{2}\frac{3}{2}}$) are overestimated by theory by almost a factor of 3. These RMEs are extremely sensitive to two-body currents, as can be seen in Table VI. The values obtained in the LWAc, LWAb and LWA2 approximations are also listed in Table VI. Similar considerations to those discussed in the previous subsection apply to these RMEs. Here we only point out that the LWAc values of the quartet E_1 RMEs are rather close to corresponding values extracted from the data (set 1). This is particularly evident when the comparison is performed directly in the observables, as can be seen from Fig. 5. In the figure, the dotted and thin solid curves are obtained in IA and by using the full current, respectively, while the thick solid curves are obtained by retaining the values calculated in the LWAc approximation for all electric dipole RMEs.

Note that for the observables σ, A_y, and iT_{11}, the contributions of the quartet E_1's are negligible. These observables depend mainly on the doublet E_1's and S-wave M_1's, and are well predicted by theory. In contrast, the observables T_{20} and T_{21} depend linearly on the quartet E_1's, and are not well reproduced by the "full"theory. The differences between the "full"and "experimental"values for these RMEs suggest that the present model for the two-body currents may have deficiencies. Note that the LWAc results for the electric dipole transitions $\overline{\mathcal{E}}_1^{1\frac{3}{2}\frac{1}{2}}$ and $\overline{\mathcal{E}}_1^{1\frac{3}{2}\frac{3}{2}}$ happen to be close to the "experimental"values, as shown in Table VI, and hence good agreement is obtained between the experimental and LWAc-calculated T_{20} and T_{21} observables. It is, however, important to emphasize that such an agreement is to be considered purely accidental, since the next to leading order contributions LWAb and LWA2 are comparable to the leading order LWAc results.

Some of the differences found between the theoretical and experimental RMEs could be due to the different elastic eigenphase shift and mixing angle parameters, used in Eq. (4.25) to define the real RMEs $\overline{\mathcal{E}}$ and $\overline{\mathcal{M}}$. To clarify this point, the elastic eigenphase shifts obtained with the AV18/UIX model are compared with those used by the authors of Ref. [9] in Table VII. There is good overall agreement between the two sets of parameters. We note that the small differences in the ^4P eigenphase shifts are responsible for the large underprediction of the A_y and iT_{11} observables in elastic *pd* scattering.

As discussed in the previous section, the LWAc and "full"estimates of the quartet E_1 RMEs are rather different (see Table II). However, when the LWAc values of these RMEs are used in evaluating the various observables, the resulting changes are found to be rather small, even for T_{20} and T_{21}. In this energy regime, the observables are in fact dominated by the doublet E_1 and the S-wave M_1 RMEs, and the contributions of the quartet E_1 RMEs are found to be negligible in all cases. At higher energies, though, the quartet E_1 becomes of the same order of magnitude of the S-wave M_1 RMEs, and therefore have large effects on some of the observables. Clearly, the significant differences between the "full"and LWAc predictions for the quartet E_1 RMEs have a large impact, particularly for the tensor observables.

Finally, in Fig. 6 the "full"results for the S-factor are compared to data in the c.m. energy range 0–2 MeV stored at the web site http://pntpm.ulb.ac.be/nacre.htm.

C. Contributions to the Gerasimov-Drell-Hearn integral

The Gerasimov-Drell-Hearn (GDH) sum rule connects the helicity structure of the photo-absorption cross section to the anomalous magnetic moment of the nuclear target, and is derived using Lorentz and gauge invariance, crossing symmetry, causality and unitarity of the forward Compton scattering amplitude [34,35]. For the case of ^{3}He, it is given by

$$I_{^3\mathrm{He}} \equiv \int_{\omega_{\mathrm{th}}}^{\infty} d\omega \frac{\sigma_P^\gamma(\omega) - \sigma_A^\gamma(\omega)}{\omega} = 2\pi^2\alpha \left(\frac{\kappa_{^3\mathrm{He}}}{m_{^3\mathrm{He}}}\right)^2 \ , \tag{4.27}$$

where $\sigma_{P/A}^\gamma(\omega)$ are the photon absorption cross sections in which the photon helicity and ^{3}He spin are either parallel (P) or antiparallel (A), $m_{^3\mathrm{He}}$ and $\kappa_{^3\mathrm{He}}$ are the ^{3}He mass and anomalous magnetic moment, and ω_{th} is the threshold energy. As discussed in the Appendix, it is related to the inclusive $R_{T'}$ response, measured in polarized electron scattering from a polarized spin 1/2 target.

In ^{3}He, the GDH integral is $I_{^3\mathrm{He}} = 498\ \mu$b, using the experimental value $\kappa_{^3\mathrm{He}} = -8.366$ for its anomalous magnetic moment. The photodisintegration threshold in ^{3}He is ω_{th}=5.495 MeV, corresponding to pd breakup. It is useful to divide the integral into the part up to pion production threshold, and the part above this threshold. For the part above pion threshold, the ^{3}He nucleus should have roughly the same strength as the neutron, i.e. $\simeq 230\ \mu$b. Such an expectation is based on the fact that the ^{3}He ground state consists predominantly of a spherically symmetric S-wave component, in which the proton spin projections are opposite and the net polarization is therefore due entirely to the neutron. Ignoring corrections to this naive estimate, it is expected that the ω-region from the photodisintegration threshold up to the pion threshold should contribute about 266 μb to the ^{3}He GDH integral. A realistic description of the pd and ppn continuum states for energies above the three-body breakup threshold in terms of PHH wave functions, while certainly possible, is not yet presently available. A calculation of the contribution to the GDH integral from the *ppn* threshold up to the pion threshold is therefore not possible. In the present work, however, we study this contribution in the 2 MeV window where only two-body photodisintegration channels are energetically allowed.

In fact, the TUNL group has recently made the first experimental determination of the contribution to the GDH integral of ^{3}He from the energy region up to 53 keV above the *pd* threshold [12]. In this region, there are only six dominant RMEs corresponding to electric and magnetic dipole transitions, as already noted before. Thus, ignoring the contributions from higher order multipoles, we find that the cross section difference in Eq. (4.27) is simply given by

$$\begin{aligned}\Delta\sigma &\equiv \sigma_P - \sigma_A \\ &= \frac{16\pi^2\alpha\mu p}{\omega}\left[-|m_2|^2 + \frac{|m_4|^2}{2} - |p_2|^2 + \frac{|p_4|^2}{2} - |q_2|^2 + \frac{|q_4|^2}{2}\right] ,\end{aligned} \tag{4.28}$$

in the notation of Eqs. (4.15)–(4.17). In particular, for the purpose of comparing with the discussion of subsection A, note the factor $1/\sqrt{2J+1}$ difference between the $\tilde{x}_{2J+1}$ and x_{2J+1} in Eq. (4.23).

As discussed in subsection A, the TUNL group has determined the relevant RMEs from an analysis of the polarized capture data, the details of which are reported in Ref. [12]. Because of time reversal invariance, the RMEs for the capture reaction are related to those for the photo-absorption reaction by phase factors, which are irrelevant for the $\Delta\sigma$ defined above.

It is convenient to define

$$I(\varpi) = \int_{\omega_{\rm th}}^{\varpi} d\omega \frac{\sigma_P(\omega) - \sigma_A(\omega)}{\omega} , \tag{4.29}$$

with, obviously, $I(\varpi \to \infty) = I_{^3{\rm He}}$. The experimental values obtained by integrating up to $\varpi_1 = 5.522$ MeV and $\varpi_2 = 5.548$ MeV are presented in Table VIII, where they are compared to predictions obtained by including one-body only and both one- and two-body currents (columns labelled IA and FULL). Note that these values represent small negative contributions to the total strength expected below pion threshold. Table VIII also lists the individual contributions to $I(\overline{\omega}_1)$ from the $-|m_2|^2+|m_4|^2/2$, $-|p_2|^2+|p_4|^2/2$, $-|q_2|^2+|q_4|^2/2$ RME combinations (rows labeled M_1, E_1 S=1/2, and E_1 S=3/2, respectively).

The total contributions including the M_1, E_1 S=1/2 and E_1 S=3/2 strengths are found to be in IA an order of magnitude smaller (in absolute value) than data. This is because in IA $|m_2|^2 \simeq 0.5 \times |m_4|^2$, $|p_2|^2 \simeq 0.5 \times |p_4|^2$ and the quartet (S=3/2) E_1 strength is very small.

The ratio $\simeq 0.5$ for the doublet to quartet M_1 strength obtained in IA is consistent with predictions for *pd* capture at zero relative energy obtained with the Faddeev method using a variety of realistic Hamiltonians [36] (the ratio is found to have only a weak energy dependence). When two-body currents are included, the doublet M_1 strength $|m_2|^2$ becomes roughly twice as large as the quartet M_1 strength $|m_4|^2$, a result also consistent with the earlier calculations [36]. This makes the overall M_1 contribution to $I(\overline{\omega})$ negative and relatively large (in absolute value).

However, the nearly exact cancellation between the doublet E_1 strengths $|p_2|^2$ and $|p_4|^2/2$ (or $|\tilde{p}_2|^2$ and $|\tilde{p}_4|^2$) discussed earlier, is not significantly influenced by the inclusion of two-body currents. The quartet E_1 RMEs remain negligible. Thus the total contribution to $I(\overline{\omega})$ is mostly due to M_1 strength. While the results in the "full"calculation are in much better agreement with data than those in IA, a factor of two discrepancy persists between theory and experiment. This discrepancy is mostly due to the difference between the calculated and measured S=1/2 E_1 strength, as the second row in Table VIII makes clear. It should also be noted that the measured $I(\overline{\omega}_2 = 5.548\text{MeV}) = -1.120 \pm 0.218$ nb is a very tiny piece of the expected contribution to the GDH integral of ^{3}He below pion threshold, i.e. 266 μb, and that it has the opposite sign.

The result for $I(\overline{\omega}_3)$ with $\overline{\omega}_3$=7.7 MeV corresponding to the threshold for complete breakup into *ppn* is 1.1 μb. We find that the cross section difference $\Delta\sigma$ changes sign in the "full"calculation at about ω=6 MeV. In the range of energy 6 MeV $\leq \omega \leq$ 7.7 MeV the polarized cross section is dominated by the $E_1^{1\frac{1}{2}J}$ RMEs. Indeed, the $|p_2|^2$ and $|p_4|^2$ strengths are three orders of magnitude larger than the strength from any of the other contributing RMEs. However, the large cancellation between $-|p_2|^2$ and $|p_4|^2/2$ persists also in this ω-region, although to a lesser extent than found above: 85% of $\Delta\sigma$ is due to these terms, while the remaining 15% comes from the other RMEs. Note that in this region, RMEs other than those included near the two-body breakup threshold need to be considered. For example, the electric quadrupole $E_2^{2\frac{1}{2}\frac{5}{2}}$ at $\omega = 7.5$ MeV ($E_p = 3$ MeV) is found to give a 4% contribution to $\Delta\sigma$.

While the results reported above indicate that an extremely tiny piece of the total sum-rule strength is located in the threshold region, we find, by direct comparison with experiment, that this integral observable is very sensitive to the effects of two-body currents. The inclusion of these currents reduces the discrepancy between theory and experiment from a factor of ten to a factor of two. Further studies are needed to understand the physical origin of the difference in the leading P-wave E_1 RMEs responsible for the remaining discrepancy.

D. Threshold electrodisintegration of ^{3}He

The most recent and systematic experimental study of the threshold electrodisintegration of ^{3}He and ^{3}H we are aware of was carried out by Retzlaff *et al.* [13] at the MIT/Bates Linear Accelerator Center. The longitudinal and transverse response functions R_L and R_T were obtained using Rosenbluth separations for three-momentum transfers in the range 0.88–2.87 fm^{-1} and excitation energies from two-body thresholds up to 18 MeV. The ^{3}H(e,e') data are the only measurements at these energy and momentum transfers. Inclusive ^{3}He electron scattering data from earlier experiments [37] are in agreement with the Retzlaff *et al.* measurements, after scaling for the slightly different kinematics.

The R_L and R_T ^{3}He data at momentum transfer values q=0.88, 1.64 and 2.47 fm^{-1} are compared in Fig. 7 with calculations using PHH wave functions obtained for the AV18/UIX Hamiltonian model, and one-body only (dashed lines) or both one- and two-body (solid lines) charge and current operators. Note that the contributions associated with the L=0–

5 *pd* scattering states are retained in the calculation, which is then fully converged. No calculations of the ^{3}H response functions have been carried out at this time. There is satisfactory agreement between theory and experiment for all cases, but for the longitudinal response at q=2.47 fm^{-1}. The two-body components of the electroexcitation operator play an important role, particularly for the transverse response at the highest q-values. The relative sign between the one- and two-body contributions is consistent with that expected from elastic form factor studies of ^{3}He. There it is found [25] that two-body current (charge) operators increase (decrease) the IA predictions for the magnetic (charge) form factor at $q \leq 3$ fm^{-1}.

A feature of the longitudinal ^{3}He data is the presence of an enhancement near threshold. Such an enhancement is particularly pronounced at low q. It is not observed in the ^{3}H longitudinal response [13]. At the momentum transfers under consideration here, the longitudinal strength is almost entirely due to a C_0 transition involving the dominant S-wave component of ^{3}He and the doublet S-wave *pd* scattering state. It has been shown by Heimback *et al.* [38] that the enhancement results from the constructive interference of the amplitudes in the two-body breakup of ^{3}He that correspond to the virtual photon coupling directly to a proton or to a correlated proton-neutron pair. In ^{3}H, the virtual photon for the two-body breakup channel can couple only to the correlated pair, since coupling directly to a proton leaves an unbound neutron pair and thus a three-body final state. The present calculations correctly account for this threshold enhancement in the longitudinal response of ^{3}He.

Previous calculations, reported on in Ref. [13], used either the Faddeev equations [39] or the orthogonal-correlated-state (OCS) method [40] to describe the bound and scattering wave functions. Both calculations did not include two-body charge and current operators. However, the former used the central Malfliet-Tjon interaction, while the latter was based on a realistic Hamiltonian including the older Argonne v_{14} two-nucleon [41] and Urbana-VII three-nucleon [42] interactions. The longitudinal and transverse response functions are surprisingly well predicted in the threshold region by the Faddeev calculation, but are both underestimated, particularly the transverse response, in the OCS calculation. The latter also fails to reproduce the observed enhancement in longitudinal strength between the two- and three-body breakup thresholds, probably because of the approximate treatment of final-state-interaction effects between the proton and deuteron clusters. However, in view of the importance of two-body currents (see Fig. 7), the agreement between the data and Faddeev results is presumably accidental.

Finally, in Figs. 8 and 9 we show the R_L, $R_{LT'}$, R_T and $R_{T'}$ response functions at a fixed excitation energy of 1 MeV above the *pd* threshold in the three-momentum transfer range 0–5 fm^{-1}. In R_L and $R_{LT'}$ the S-wave *pd* continuum states give the dominant contribution, while in R_T and $R_{T'}$ both S- and P-wave states give equally important contributions over the whole q range. All response functions are substantially affected by two-body currents, however, the sensitivity to these is particularly pronounced for $R_{LT'}$ and $R_{T'}$.

In Fig. 10 we show the unpolarized cross section, and the $A_{LT'}$ and $A_{T'}$ asymmetries in the threshold region at an incident electron energy of 4 GeV. The asymmetries are relatively large at high q, and particularly sensitive to two-body currents. Note that $A_{LT'}$ has been found to be little influenced by uncertainties in the electric form factor of the neutron (the Galster parametrization is used in Figs. 7–10), except at the highest q-values. The cross section for the chosen kinematics (incident electron energy of 4 GeV, fixed *pd* excitation energy of 1 MeV, and $0^\circ < \theta_e < 14^\circ$) is dominated by the longitudinal response function. Note that in Fig. 10 we also show the plane-wave-impulse-approximation (PWIA) results. These have been calculated by approximating the wave function

$$\Psi_{1+2}^{LSJJ_z}(\text{PWIA}) = \sum_{\text{cyclic}\, ijk} \Big[[s_i \otimes \phi_d(\mathbf{x}_i)]_S \otimes Y_L(\hat{\mathbf{y}}_i) \Big]_{JJ_z} \frac{F_L(pr_{pd})}{pr_{pd}} \ . \tag{4.30}$$

The lack of orthogonality between the $\Psi_{1+2}^{LSJJ_z}(\text{PWIA})$ with $L = 0$ $S = 1/2$ and the ^{3}He ground-state wave functions is responsible for the excess cross section at low q obtained in PWIA with respect to the "full"calculation.

V. CONCLUSIONS

We have reported calculations of *pd* radiative capture observables at energies below the three-body breakup threshold, and of longitudinal, transverse and interference response functions measured in polarized electron scattering from polarized ^{3}He in the threshold region for momentum transfers in the range 0–5 fm^{-1}. These calculations have been based on the Argonne v_{18} two-nucleon [10] and Urbana-IX three-nucleon [11] interactions, and have used accurate bound and continuum wave functions, obtained with the PHH method [2,3,14]. The model for the electromagnetic operator has been taken to consist of one- and two-body components, the latter ones constructed consistently with the two-nucleon interaction [19,25]. In recent studies, this theory has been shown to correctly predict the static properties of the trinucleons [25] and $A = 6$ nuclei [43], as well as their associated elastic and transition electromagnetic form factors.

A satisfactory description of all measured *pd* observables has emerged with the exception of the differential cross section and tensor analyzing power at small angles for $E_p < 40$ keV, and the contributions to the GDH integral at energies in the c.m. range 0–53 keV. A comparison between the calculated RMEs and those extracted from fits to the measured data has shown that the large p_4 RME associated with the channel $L, S, J = 1, 1/2, 3/2$ is overestimated by theory at very low energy. It has been speculated that at these energies (below $\leq$ 50 keV) long-range electromagnetic interactions beyond the static Coulomb repulsion between protons might play a role. These electromagnetic interactions have already been included in bound-state calculations (such as those reported here), where they have been found to contribute to ground-state energy differences between mirror nuclei or members of isomultiplets [4]. However, they have yet to be included in scattering-state calculations. Work along these lines is currently underway. It should emphasized that at higher energies the splitting between the p_2 and p_4 RMEs appears to be much reduced, as the fits to the *pd* observables at 2 MeV indicate. This result is further corroborated by a phase shift analysis of *pd* elastic scattering at energies below the *ppn* breakup threshold [5], which leads to very close values for the $^2P_{1/2}$ and $^2P_{3/2}$ phases. At 2 MeV the tensor observables T_{20} and T_{21} are sensitive to the "small"quartet E_1 RMEs. The "full"calculation fails to correctly predict these observables, suggesting that the present model for the electromagnetic transition operator may have deficiencies. Finally, the validity of the long-wavelength approximation has been analyzed. This approximation has been found to be inadequate for the calculation of inhibited (and hence "small") electric dipole transitions. Model calculations of low-energy capture and photodisintegration observables, based on the long-wavelength form of the E_1 operator (the LWAc operator of Eq. (4.8)), should therefore be viewed with suspicion unless explicitely verifying that higher order corrections are indeed negligible.

The body of data available from ^{3}He(e, e') inclusive scattering experiments in the threshold region is not as extensive, at present, as that from *pd* capture experiments. However, polarized electron scattering data from a polarized ^{3}He target below the *ppn* threshold should become available in the near future [44]. The longitudinal and transverse data measured at Bates by the Saskatoon group are in reasonable agreement with theory, although the data have rather large errors. The crucial role played by two-body charge and current operators should be re-emphasized.

ACKNOWLEDGMENTS

The authors wish to thank J.L. Friar for clarifications concerning the long-wavelength approximation to electric dipole transitions, L.D. Knutson for useful discussions, and L.D. Knutson, D. Skopik, H.R. Weller and E.A. Wulf for allowing them the use of their data. R.S. also thanks W. Boeglin for a series of interesting discussions. M.V. and R.S. acknowledge partial financial support of NATO through the Collaborative Research Grant No. 930741. The support of the U.S. Department of Energy under contract number DE-AC05-84ER40150 is gratefully acknowledged by L.E.M. and R.S. Finally, some of the calculations were made possible by grants of time from the National Energy Research Supercomputer Center in Livermore.

APPENDIX A: EXPRESSIONS OF OBSERVABLES IN TERMS OF REDUCED MATRIX ELEMENTS

Expressions for the angular distributions of the cross section, vector and tensor analyzing powers and photon linear polarization coefficient were derived in terms of reduced matrix elements of electric and magnetic multipole operators in Ref. [6]. It it useful to extend that analysis also to the case of the threshold photo- and electro-disintegration of ^{3}He, since at the the small excitation energies of interest here only a relatively small number of electromagnetic multipoles are expected to contribute significantly.

The electromagnetic transition amplitudes between an initial ^{3}He bound state with spin projection σ_3 and a final pd continuum state having proton and deuteron with relative momentum $\mathbf{p}$ and spin projections, respectively, σ_2 and σ, are given by:

$$\rho_{\sigma\sigma_2\sigma_3}(\mathbf{p},\mathbf{q}) = \langle \Psi^{(-)}_{\mathbf{p},\sigma\sigma_2} | \rho(\mathbf{q}) | \Psi_{3,\frac{1}{2}\sigma_3} \rangle \ , \tag{A1}$$

$$j^{\lambda}_{\sigma\sigma_2\sigma_3}(\mathbf{p},\mathbf{q}) = \langle \Psi^{(-)}_{\mathbf{p},\sigma\sigma_2} | \hat{\epsilon}_\lambda(\mathbf{q}) \cdot \mathbf{j}(\mathbf{q}) | \Psi_{3,\frac{1}{2}\sigma_3} \rangle \ , \tag{A2}$$

where $\mathbf{q}$ is the momentum transfer and $\hat{\epsilon}_\lambda(\mathbf{q})$, $\lambda = \pm 1$, are the transverse polarizations of the (real or virtual) photon. The wave function with ingoing-wave boundary condition is expanded as

$$\Psi^{(-)}_{\mathbf{p},\sigma\sigma_2} = 4\pi \sum_{SS_z} \langle \frac{1}{2}\sigma, 1\sigma_2 | SS_z \rangle \sum_{LL_zJJ_z} \mathrm{i}^L \, \langle SS_z, LL_z | JJ_z \rangle Y^*_{LL_z}(\hat{\mathbf{p}}) \overline{\Psi}^{LSJJ_z(-)}_{1+2} \ , \tag{A3}$$

where the $\overline{\Psi}^{LSJJ_z(-)}_{1+2}$ are related to the $\Psi^{LSJJ_z}_{1+2}$ introduced in Sec. II via

$$\overline{\Psi}^{LSJJ_z(-)}_{1+2} = \mathrm{e}^{-\mathrm{i}\sigma_L} \sum_{L'S'} \left[1 + \mathrm{i}\, R^J \right]^{-1}_{LS,L'S'} \Psi^{L'S'JJ_z}_{1+2} \ . \tag{A4}$$

Here σ_L is the Coulomb phase shift and R^J is the R-matrix. Introducing the expansion above into the matrix elements, Eqs. (A1)–(A2), one finds:

$$j^{\lambda}_{\sigma\sigma_2\sigma_3}(\mathbf{p},\mathbf{q}) = 4\pi \sum_{LL_zSS_zJJ_z} (-\mathrm{i})^L \langle \frac{1}{2}\sigma, 1\sigma_2 | SS_z \rangle \langle SS_z, LL_z | JJ_z \rangle Y_{LL_z}(\hat{\mathbf{p}}) \, j^{LSJ}_{J_z\lambda\sigma_3}(\mathbf{q}) \ , \tag{A5}$$

$$j^{LSJ}_{J_z\lambda\sigma_3}(\mathbf{q}) = \langle \overline{\Psi}^{LSJJ_z(-)}_{1+2} | \hat{\epsilon}_\lambda(\mathbf{q}) \cdot \mathbf{j}(\mathbf{q}) | \Psi_{3,\frac{1}{2}\sigma_3} \rangle \ , \tag{A6}$$

and similar expressions hold for the $\rho_{\sigma\sigma_2\sigma_3}(\mathbf{p},\mathbf{q})$ amplitudes. It is now convenient to take $\hat{\mathbf{q}}$ as defining the z-axis, i.e. the spin-quantization axis. Standard techniques [45] then lead to the following expansions in terms of reduced matrix elements of Coulomb (C), electric (E) and magnetic (M) multipoles for the amplitudes $\rho^{LSJ}_{J_z\sigma_3}(\mathbf{q})$ and $j^{LSJ}_{J_z\lambda\sigma_3}(\mathbf{q})$:

$$\rho^{LSJ}_{J_z\sigma_3}(q\hat{\mathbf{z}}) = \sqrt{4\pi} \sum_{\ell=0}^{\infty} \mathrm{i}^\ell \sqrt{\frac{2\ell+1}{2J+1}} \langle \frac{1}{2}\sigma_3, \ell 0 | J J_z \rangle \ C^{LSJ}_\ell(q) \ , \tag{A7}$$

$$j^{LSJ}_{J_z\lambda\sigma_3}(q\hat{\mathbf{z}}) = -\sqrt{2\pi} \sum_{\ell=1}^{\infty} \mathrm{i}^\ell \sqrt{\frac{2\ell+1}{2J+1}} \langle \frac{1}{2}\sigma_3, \ell\lambda | J J_z \rangle \ [\lambda M^{LSJ}_\ell(q) + E^{LSJ}_\ell(q)] \ . \tag{A8}$$

The matrix elements $\rho^{LSJ}_{J_z\sigma_3}(q\hat{\mathbf{z}})$ and $j^{LSJ}_{J_z\lambda\sigma_3}(q\hat{\mathbf{z}})$ are calculated with the Monte Carlo integration techniques discussed in Ref. [6], and from these the reduced matrix elements $C^{LSJ}_\ell(q)$, $M^{LSJ}_\ell(q)$ and $E^{LSJ}_\ell(q)$ are obtained via Eqs. (A7)–(A8), for example

$$C^{LS\frac{1}{2}}_0(q) = \frac{1}{\sqrt{2\pi}} \rho^{LS\frac{1}{2}}_{\frac{1}{2}\frac{1}{2}}(q\hat{\mathbf{z}}) \ , \tag{A9}$$

$$M^{LS\frac{3}{2}}_1(q) = \frac{\mathrm{i}}{\sqrt{2\pi}} \left[\sqrt{3} j^{LS\frac{3}{2}}_{\frac{3}{2}1\frac{1}{2}}(q\hat{\mathbf{z}}) - j^{LS\frac{3}{2}}_{-\frac{1}{2}-1\frac{1}{2}}(q\hat{\mathbf{z}}) \right] \ . \tag{A10}$$

The inclusive cross section for polarized electron scattering from a polarized spin 1/2 target can simply be written as [46]

$$\frac{d^3\sigma}{d\Omega d\omega} = \Sigma(q,\omega) + h \ \Delta(q,\omega) \ , \tag{A11}$$

$$\Sigma(q,\omega) = \sigma_M [v_L R_L(q,\omega) + v_T R_T(q,\omega)] \ , \tag{A12}$$

$$\Delta(q,\omega) = \sigma_M [v_{LT'} R_{LT'}(q,\omega) \sin\theta^* \cos\phi^* + v_{T'} R_{T'}(q,\omega) \cos\theta^*] \ , \tag{A13}$$

where σ_M is the Mott cross section, the coefficients v_α are functions of the electron kinematic variables, $h = \pm 1$ is the helicity of the incident electron, and the angles θ^* and ϕ^* specify the direction of the target polarization with respect to $\hat{\mathbf{q}}$. The response functions R_α contain the nuclear structure information. We note that the sum over the three-nucleon final states, implicit in their definition, is restricted to include only the *pd* continuum, since the excitation energies of interest here are below the threshold for the three-body breakup. The longitudinal-transverse and transverse-transverse asymmetries $A_{LT'}$ and $A_{T'}$ are defined as:

$$A_{LT'}(q,\omega) = \frac{v_{LT'} R_{LT'}(q,\omega)}{v_L R_L(q,\omega) + v_T R_T(q,\omega)} ,$$
$$A_{T'}(q,\omega) = \frac{v_{T'} R_{T'}(q,\omega)}{v_L R_L(q,\omega) + v_T R_T(q,\omega)} . \tag{A14}$$

Explicit expressions for the response functions R_α in terms of reduced matrix elements of electromagnetic multipole operators are easily obtained:

$$R_L = f_{pd} \sum_{LSJ\ell} |C_\ell^{LSJ}|^2 , \tag{A15}$$

$$R_T = f_{pd} \sum_{LSJ\ell} (|E_\ell^{LSJ}|^2 + |M_\ell^{LSJ}|^2) , \tag{A16}$$

$$R_{LT'} = 2\sqrt{2}\, f_{pd} \sum_{LSJ} \frac{\sqrt{J+1/2}}{2J+1} \Re\Big[\Big(C_-^{LSJ} + \mathrm{i}\, C_+^{LSJ} \Big)^* \Big[\sqrt{J-1/2}\,(M_-^{LSJ} + E_-^{LSJ}) - \mathrm{i}\sqrt{J+3/2}\,(M_+^{LSJ} + E_+^{LSJ})\Big]\Big] , \tag{A17}$$

$$R_{T'} = 2\, f_{pd} \sum_{LSJ} \frac{1}{2J+1} \Big[|M_-^{LSJ} + E_-^{LSJ}|^2 - |M_+^{LSJ} + E_+^{LSJ}|^2 - 2\sqrt{(J+3/2)(J-1/2)}\, \Im\Big[(M_-^{LSJ} + E_-^{LSJ})^*(M_+^{LSJ} + E_+^{LSJ})\Big]\Big] , \tag{A18}$$

where the phase-space factor f_{pd} is given by $f_{pd} = 4\mu p$, and in the interference response functions the notation $X_\pm^{LSJ}$ for the reduced matrix elements means $X_{\ell=J\pm1/2}^{LSJ}$. The magnitude of the relative momentum p is fixed by energy conservation

$$\omega + E_3 = E_2 + \frac{q^2}{2(m_2+m)} + \frac{p^2}{2\mu} , \tag{A19}$$

where E_2 and E_3 are the two- and three-body ground-state energies, m_2 is the deuteron mass and μ is the 1+2 reduced mass.

The photo-disintegration cross section is simply related to the R_T response function:

$$\sigma^{\gamma}(\omega) = \frac{4\pi^2\alpha}{\omega} R_T(\omega) \ , \tag{A20}$$

where for real photons $q = \omega$. In particular, the difference of cross sections in the integrand of Eq.(4.27) is easily related to the response function $R_{T'}$

$$\sigma_P^{\gamma}(\omega) - \sigma_A^{\gamma}(\omega) = \frac{4\pi^2\alpha}{\omega} R_{T'}(\omega) \ . \tag{A21}$$

REFERENCES

[1] W. Glöckle *et al.*, Phys. Rep. **274**, 107 (1996).

[2] A. Kievsky, M. Viviani, and S. Rosati, Nucl. Phys. **A577**, 511 (1994).

[3] A. Kievsky, M. Viviani, and S. Rosati, Phys. Rev. C **52**, R15 (1995).

[4] B.S. Pudliner *et al.*, Phys. Rev. C **56**, 1720 (1997).

[5] A. Kievsky, S. Rosati, W. Tornow, and M. Viviani, Nucl. Phys. **A607**, 402 (1996).

[6] M. Viviani, R. Schiavilla, and A. Kievsky, Phys. Rev. C **54**, 534 (1996).

[7] G.J. Schmid *et al.*, Phys. Rev. Lett. **76**, 3088 (1996).

[8] L. Ma *et al.*, Phys. Rev. C **55**, 588 (1997).

[9] M.K. Smith and L.D. Knutson, Phys. Rev. Lett. **82**, 4591 (1999).

[10] R.B. Wiringa, V.G.J. Stoks, and R. Schiavilla, Phys. Rev. C **51**, 38 (1995).

[11] B.S. Pudliner, V.R. Pandharipande, J. Carlson, and R.B. Wiringa, Phys. Rev. Lett. **74**, 4396 (1995).

[12] E.A. Wulf *et al.*, Phys. Rev. C in press.

[13] G.A. Retzlaff *et al.*, Phys. Rev. C **49**, 1263 (1994).

[14] A. Kievsky, M. Viviani, and S. Rosati, Nucl. Phys. **A551**, 241 (1993).

[15] A. Kievsky *et al.*, Phys. Rev. C **58**, 3085 (1998).

[16] T. deForest and J.D. Walecka, Adv. Phys. **15**, 1 (1966).

[17] J.L. Friar, Ann. Phys. (N.Y.) **81**, 332 (1973).

[18] S. Galster, *et al.*, Nucl. Phys. **B32**, 221 (1971).

[19] J. Carlson and R. Schiavilla, Rev. Mod. Phys. **70**, 743 (1998).

[20] D.O. Riska, Phys. Rep. **181**, 207 (1989).

[21] D.O. Riska, Phys. Scr. **31**, 471 (1985).

[22] H. Berg *et al.*, Nucl. Phys. **A334**, 21 (1980).

[23] M. Chemtob and M. Rho, Nucl. Phys. **A163**, 1 (1971); **A212**, 628(E) (1973).

[24] R. Schiavilla, R.B. Wiringa, V.R. Pandharipande, and J. Carlson, Phys. Rev. C **45**, 2628 (1992).

[25] L.E. Marcucci, D.O. Riska, and R. Schiavilla, Phys. Rev. C **58**, 3069 (1998).

[26] C.E. Carlson, Phys. Rev. D **34**, 2704 (1986).

[27] D. Lin and M.K. Liou, Phys. Rev. C **43**, R930 (1991).

[28] M. Garçon, private communication (1999).

[29] R. Schiavilla, V.R. Pandharipande, and D.O. Riska, Phys. Rev. C **41**, 309 (1990).

[30] J.L. Friar and S. Fallieros, Phys. Lett. **114B**, 403 (1982). Note that Eqs. (4.4)–(4.6) in the present work coincide with Eq. (8b) of the Friar and Fallieros paper above. However, this is not the "optimal "form of the E_1 operator advocated by these authors. It is, however, equivalent to it when conserved currents are used.

[31] E.A. Wulf and H.R. Weller, private communication.

[32] K.M. Watson, Phys. Rev. **95**, 228 (1954).

[33] B.J. Rice *et al.*, Phys. Rev. C **56**, R2917 (1997).

[34] S.B. Gerasimov, Yad. Fiz. **2**, 598 (1965) [Sov. J. Nucl. Phys. **2**, 430 (1966)].

[35] S.D. Drell and A.C. Hearn, Phys. Rev. Lett. **16**, 908 (1966).

[36] J.L. Friar *et al.*, Phys. Rev. Lett. **66**, 1827 (1991).

[37] R.F. Frosch *et al.*, Phys. Lett. 24**B**, 54 (1967); B.T. Chertok *et al.*, Phys. Rev. Lett.

23, 34 (1969); P.T. Kan *et al.*, Phys. Rev. C **12**, 1118 (1975); G. Köbschall *et al.*, Nucl. Phys. **A412**, 294 (1983).

[38] C.R. Heimbach, D.R. Lehman, and J.S. O'Connell, Phys. Rev. C **16**, 2135 (1977).

[39] E. van Meijgaard and J.A. Tjon, Phys. Rev. C **45**, 1463 (1992).

[40] R. Schiavilla and V.R. Pandharipande, Phys. Rev. C **36**, 2221 (1987); R. Schiavilla, Phys. Lett. **B218**, 1 (1989).

[41] R.B. Wiringa, R.A. Smith, and T.L. Ainsworth, Phys. Rev. C **29**, 1207 (1984).

[42] R. Schiavilla, V.R. Pandharipande, and R.B. Wiringa, Nucl. Phys. **A449**, 219 (1986).

[43] R.B. Wiringa and R. Schiavilla, Phys. Rev. Lett. **81**, 4317 (1998).

[44] H. Gao, private communication (1999).

[45] J.D. Walecka, *Theoretical Nuclear and Subnuclear Physics* (Oxford University Press, New York, 1995).

[46] T.W. Donnely and A.S. Raskin, Ann. Phys. (N.Y.) **169**, 247 (1986).

TABLES

	a_2 (fm)		a_4 (fm)	
	Th	Exp	Th	Exp
nd	0.63	0.65 ± 0.04	6.33	6.35 ± 0.02
pd	-0.02		13.7	

TABLE I. Predictions obtained from the AV18/UIX Hamiltonian model with the PHH method for the *nd* and *pd* doublet and quartet scattering lengths a_2 and a_4.

	IA	FULL	LWAc	LWAb	LWA2
$\widetilde{E}_{1C}^{1\frac{1}{2}\frac{1}{2}}$	-24.2	-26.2	-26.0	-0.1	0.1
$\widetilde{E}_{1C}^{1\frac{3}{2}\frac{1}{2}}$	-6.1	0.6	2.1	0.6	-0.4
$\widetilde{E}_{1C}^{1\frac{1}{2}\frac{3}{2}}$	33.1	36.7	36.9	0.0	0.1
$\widetilde{E}_{1C}^{1\frac{3}{2}\frac{3}{2}}$	-2.7	0.1	0.6	-1.3	0.7

TABLE II. Doublet and quartet E_1 RMEs in $\mathrm{fm}^{3/2}$ calculated with the AV18/UIX Hamiltonian model for the reaction ^{2}H(p,γ)^{3}He at zero energy in IA and FULL approximations. The contributions LWAc, LWAb, and LWA2 are reported in columns 4–6, see text for an explanation. Note that the LWA2 contribution has been calculated by using only the magnetization term of the single-nucleon current, i.e. by only retaining the second term on the r.h.s. of Eq. (3.6). Statistical errors associated with the Monte Carlo integrations are in the range 1–5%.

RME	IA	FULL	FIT
$\|\tilde{m}_2\|$	0.172	0.322	0.340±0.010
$\|\tilde{m}_4\|$	0.174	0.157	0.157±0.007
$\|\tilde{p}_2\|$	0.346	0.371	0.363±0.014
$\|\tilde{p}_4\|$	0.343	0.378	0.312±0.009

TABLE III. Magnitudes of the leading M_1 and E_1 RMEs for *pd* capture at $E_p = 40$ keV. The values listed in the fourth column have been determined in Ref. [12] from a fit to the measured observables, while those listed in the second and third columns have been obtained in calculations using either one-body (IA) only or both one- and two-body (FULL) currents. Note that the RMEs listed in this table are adimensional.

E_p(MeV)	$^2P_{1/2}$	$^2P_{3/2}$
0.035	–0.00392	–0.00391
0.213	–0.699	–0.695
2.0	–4.89	–4.84
3.0	–7.37	–7.17
3.0 (PSA)	–7.41(0.08)	–7.18(0.04)

TABLE IV. Nuclear elastic *pd* phase shifts (in degrees) obtained for a few selected proton energies with the AV18/UIX Hamiltonian model. The values extracted from the phase-shift analysis (PSA) of Ref. [5] are listed in the last row.

RME	set 1	set 2	AV18/UIX
$\overline{\mathcal{M}}_1^{0\frac{1}{2}\frac{1}{2}}$	−0.221		−0.243
$\overline{\mathcal{M}}_1^{2\frac{3}{2}\frac{1}{2}}$		−0.355	0.023
$\overline{\mathcal{M}}_1^{0\frac{3}{2}\frac{3}{2}}$	−0.221	−0.220	−0.192
$\overline{\mathcal{M}}_1^{2\frac{1}{2}\frac{3}{2}}$	0.272	0.476	0.018
$\overline{\mathcal{M}}_1^{2\frac{3}{2}\frac{3}{2}}$	0.184	0.324	0.019
$\overline{\mathcal{E}}_1^{1\frac{1}{2}\frac{1}{2}}$	2.721	2.434	2.678
$\overline{\mathcal{E}}_1^{1\frac{3}{2}\frac{1}{2}}$	−0.122	−0.118	−0.308
$\overline{\mathcal{E}}_1^{1\frac{1}{2}\frac{3}{2}}$	2.742	2.717	2.771
$\overline{\mathcal{E}}_1^{1\frac{3}{2}\frac{3}{2}}$	0.080	0.061	0.175
$\overline{\mathcal{E}}_1^{3\frac{3}{2}\frac{3}{2}}$	0.061	0.085	0.072

TABLE V. Real RMEs ($\times 10^3$) for *pd* radiative capture at $E_{\rm c.m.}$ = 2 MeV, see text for definitions. Sets labelled 1 and 2 are the RMEs obtained in Ref. [9] from a fit to the measured observables. The RMEs in the column labelled AV18/UIX have been obtained by the calculation presented in this paper, including the full current operator. Note that the RMEs defined in this table are adimensional.

RME	set 1	IA	FULL	LWAc	LWAb	LWA2
$\overline{\mathcal{E}}_1^{1\frac{1}{2}\frac{1}{2}}$	2.721	2.352	2.678	2.699	0.012	–0.021
$\overline{\mathcal{E}}_1^{1\frac{3}{2}\frac{1}{2}}$	–0.122	–1.166	–0.308	–0.127	0.071	–0.050
$\overline{\mathcal{E}}_1^{1\frac{1}{2}\frac{3}{2}}$	2.742	2.395	2.771	2.716	–0.042	0.011
$\overline{\mathcal{E}}_1^{1\frac{3}{2}\frac{3}{2}}$	0.080	0.405	0.175	0.111	0.121	–0.069
$\overline{\mathcal{E}}_1^{3\frac{3}{2}\frac{3}{2}}$	0.061	0.069	0.072	0.070	0.002	0.001

TABLE VI. Real RMEs ($\times 10^3$) for *pd* radiative capture at $E_{\rm c.m.} = 2$ MeV as in Table V. Set 1 are the RMEs obtained in Ref. [9] from a fit to the measured observables. The RMEs in the columns labelled IA, FULL, LWAc, LWAb, and LWA2 have been obtained in calculations using various approximations for the E_1 operator as in Table II. Note that the RMEs defined in this table are adimensional.

wave	δ^{LSJ} Exp (deg)	δ^{LSJ} AV18/UIX (deg)
$^2S_{1/2}$	−24.9	−27.9
$^4D_{1/2}$	4.27	4.27
$^4S_{3/2}$	116.1	116.9
$^2D_{3/2}$	9.83	9.98
$^4D_{3/2}$	4.12	4.01
$^2P_{1/2}$	−1.82	−2.15
$^4P_{1/2}$	26.9	27.4
$^2P_{3/2}$	−1.95	−1.95
$^4P_{3/2}$	29.4	29.3
$^4F_{3/2}$	10.4	10.4

TABLE VII. Eigenphase shifts δ^{LSJ} for *pd* elastic scattering at $E_{\rm c.m.} = 2$ MeV. The values of LSJ are given in column 1 in the format $^{2S+1}L_J$. The experimental phase shifts are those from Ref. [9], whereas the theoretical ones are calculated with the AV18/UIX interaction model. The values reported here are the phase shifts induced in the wave functions by the nuclear plus Coulomb potential.

$\overline{\omega}$ (MeV)	$I(\overline{\omega})$	FIT	IA	FULL
5.522	M_1	-0.0524 ± 0.0077	-0.0029	-0.0609
5.522	E_1 S =1/2	-0.0361 ± 0.0095	-0.0030	$+0.0027$
5.522	E_1 S =3/2	-0.0026 ± 0.0007	-0.0050	-0.0001
5.522	Total	-0.0911 ± 0.0123	-0.0109	-0.0583
5.548	Total	-1.120 ± 0.218	-0.161	-0.582

TABLE VIII. The contributions $I(\overline{\omega})$ (in nb) for two energies $\overline{\omega}$. In the third column, the values obtained from a fit of the experimental *pd* capture data are reported [12]. The results of the theoretical calculations using the AV18/UIX Hamiltonian model and either one-body only or both one- and two-body currents are listed in the fourth and fifth columns, labelled IA and FULL respectively. The lines denoted by M_1, E_1 S=1/2 and E_1 S=3/2 report the partial contributions to $I(\overline{\omega}$=5.522 MeV) of the corresponding RMEs.

FIGURES

FIG. 1. The S-factor for the ^{2}H$(p,\gamma)^3$He reaction, obtained with the AV18/UIX Hamiltonian model and one-body only (dashed line) or both one- and two-body (solid line) currents, is compared with the experimental values of Refs. [7,8].

FIG. 2. The energy integrated cross section $\sigma(\theta)/a_0$ ($4\pi a_0$ is the total cross section), vector analyzing power $A_y(\theta)$, tensor analyzing power $T_{20}(\theta)$ and photon linear polarization coefficient $P_\gamma(\theta)$ obtained with the AV18/UIX Hamiltonian model and one-body only (dashed line) or both one- and two-body (solid line) currents are compared with the experimental results of Ref. [7].

FIG. 3. The functions $\Re[\tilde{p}_{2J+1}(r_{pd})]$ calculated with the AV18/UIX Hamiltonian model for the states $J = 1/2$ and $3/2$. The functions obtained by switching off the nuclear pd intercluster interactions are displayed by the thin dashed and solid lines for the $J = 1/2$ and $J = 3/2$ scattering states, respectively. The two lines are indistinguishable. When the nuclear interactions between the d and p clusters are taken into account, the functions are shown by the thick dashed and solid lines for the $J = 1/2$ and $J = 3/2$ scattering states, respectively.

FIG. 4. Proton vector analyzing power A_y and deuteron tensor analyzing power T_{20} for pd capture at $E_{\text{c.m.}} = 75$ and 100 keV, obtained with the AV18/UIX Hamiltonian model and one-body only (dashed lines) or both one- and two-body currents (solid lines). The experimental values are from Ref. [8].

FIG. 5. Differential cross section, proton vector analyzing power, and the four deuteron tensor analyzing powers for pd capture at $E_{\text{c.m.}} = 2$ MeV, obtained with the AV18/UIX Hamiltonian model and one-body only (dashed lines) or both one- and two-body currents (thin solid lines), are compared with the experimental values of Ref. [9]. The results obtained in the approximation LWAc for the E_1 operator are also shown (solid lines).

FIG. 6. The S-factor for the ^{2}H$(p,\gamma)^3$He reaction, in the c.m. energy range $0-2$ MeV, obtained with the AV18/UIX Hamiltonian model and one- and two-body currents (solid line) is compared with the experimental values listed in the web site `http://pntpm.ulb.ac.be/nacre.htm`.

FIG. 7. The longitudinal and transverse response functions of ^{3}He, obtained with the AV18/UIX Hamiltonian model and one-body only (dashed lines) or both one- and two-body (solid lines) charge and current operators, are compared with the data of Ref. [13] at excitation energies below the *ppn* breakup threshold.

FIG. 8. The longitudinal (R_L) and longitudinal-transverse ($R_{LT'}$) response functions of ^{3}He, obtained with the AV18/UIX Hamiltonian model and one-body only (thick dashed lines) or both one- and two-body (thick solid lines) charge and current operators, are displayed at a fixed excitation energy of 1 MeV for three-momentum transfers in the range 0–5 fm^{-1}. The contributions associated with the (dominant) S-wave *pd* scattering states are also shown.

FIG. 9. Same as in Fig. 8, but for the transverse (R_T) and transverse-transverse ($R_{T'}$) response functions of ^{3}He. The contributions associated with both S- and P-wave *pd* scattering states are also shown.

FIG. 10. The inclusive cross section, and the $A_{LT'}$ and $A_{T'}$ asymmetries, obtained with the AV18/UIX Hamiltonian model and one-body only (dashed lines) or both one- and two-body (solid lines) charge and current operators, are displayed for ^{3}He at a fixed excitation energy of 1 MeV for three-momentum transfers in the range 0–5 fm^{-1}. The results in PWIA (dotted lines) are also shown. The incident electron energy is 4 GeV, and the electron scattering angle is in the range 0–14°.

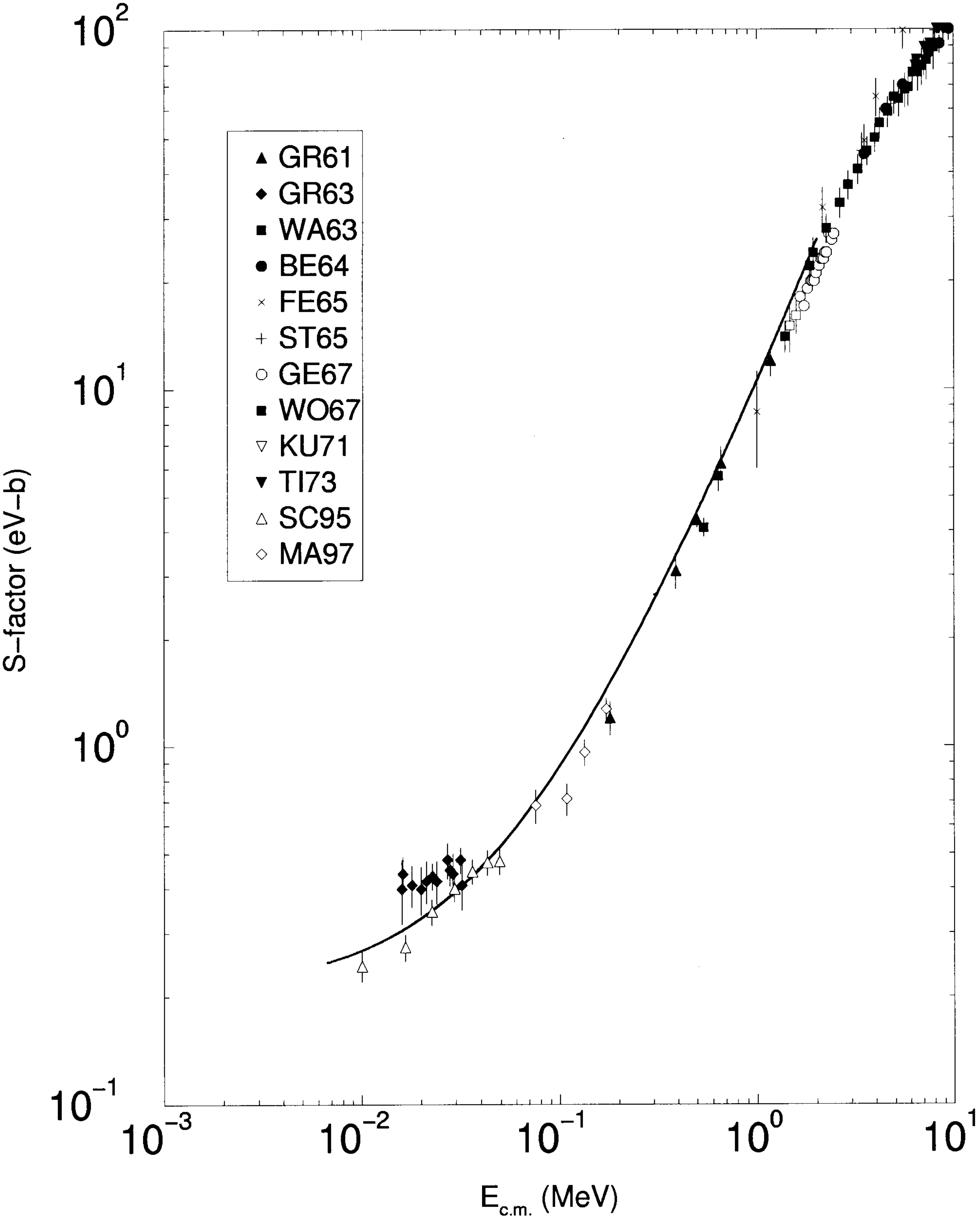

GR61
GR63
WA63
BE64
FE65
ST65
GE67
WO67
KU71
TI73
SC95
MA97
S–factor (eV–b)
10^{2}
10^{1}
10^{0}
10^{-1}
10^{-3}
10^{-2}
10^{-1}
10^{0}
10^{1}
$E_{c.m.}$ (MeV)

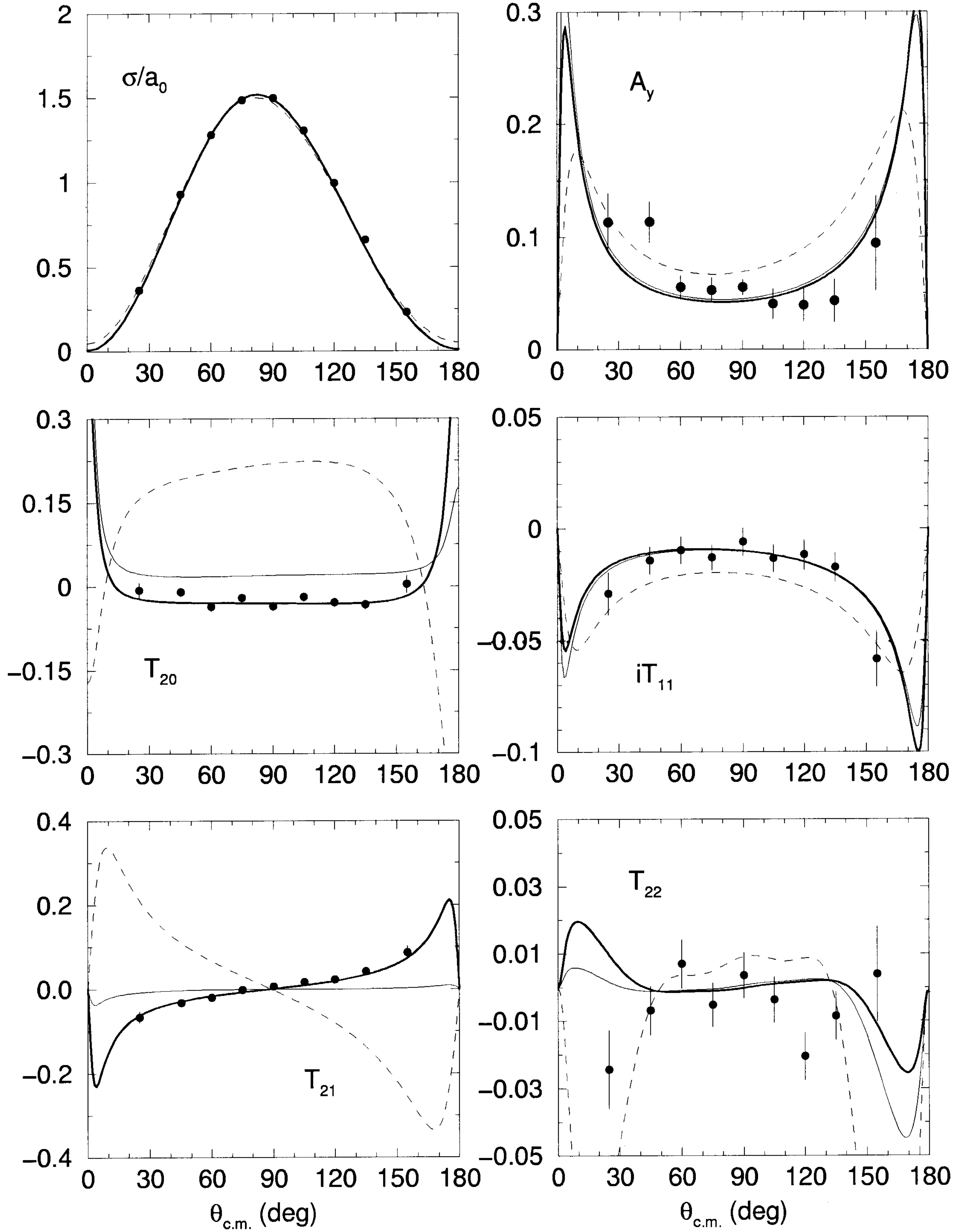
σ/a₀
A_y
T_20
iT_11
T_21
T_22
θ_c.m. (deg)
θ_c.m. (deg)

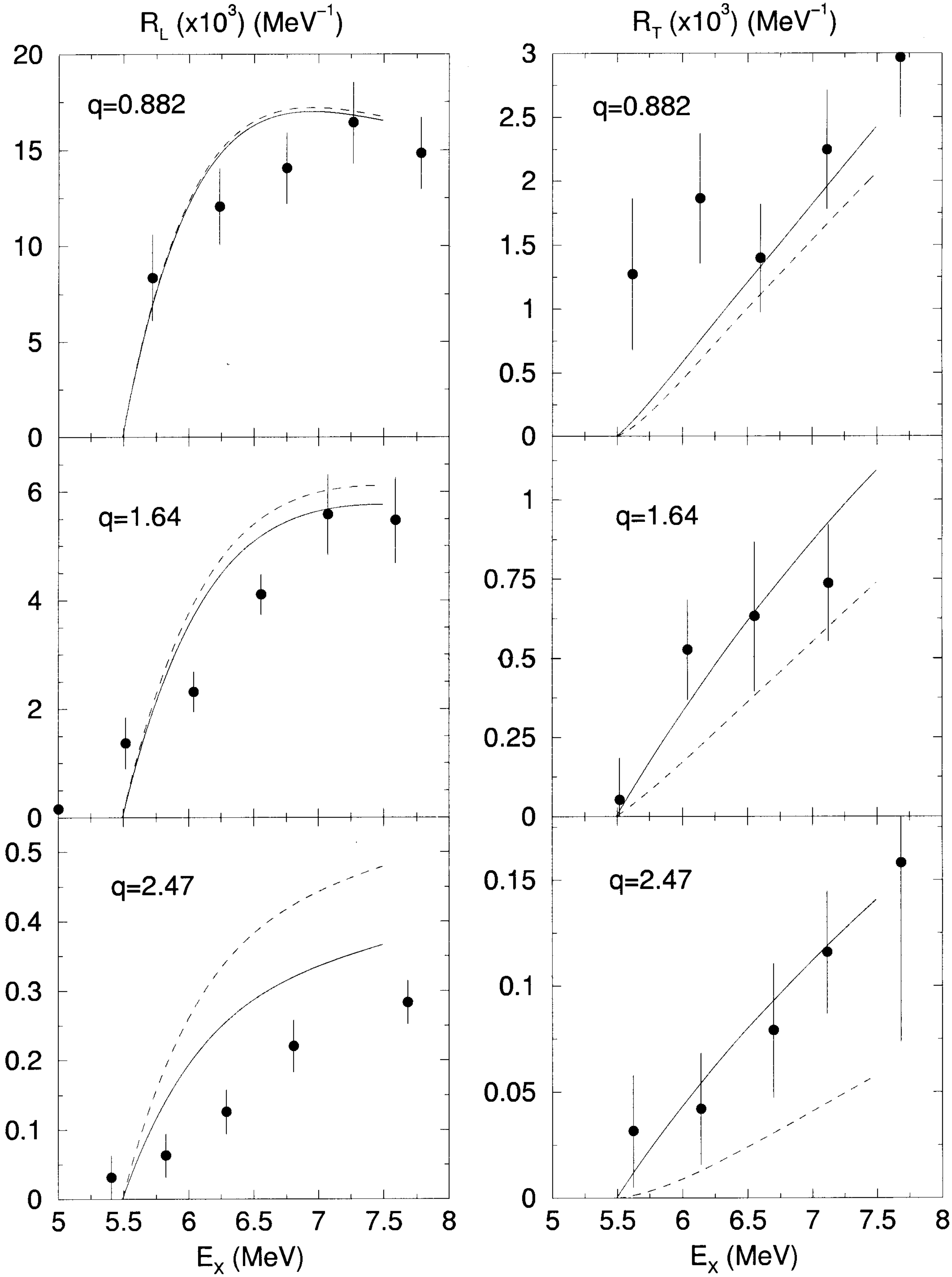

R_L (x10^3) (MeV^-1)
R_T (x10^3) (MeV^-1)
q=0.882
q=1.64
q=2.47
E_X (MeV)

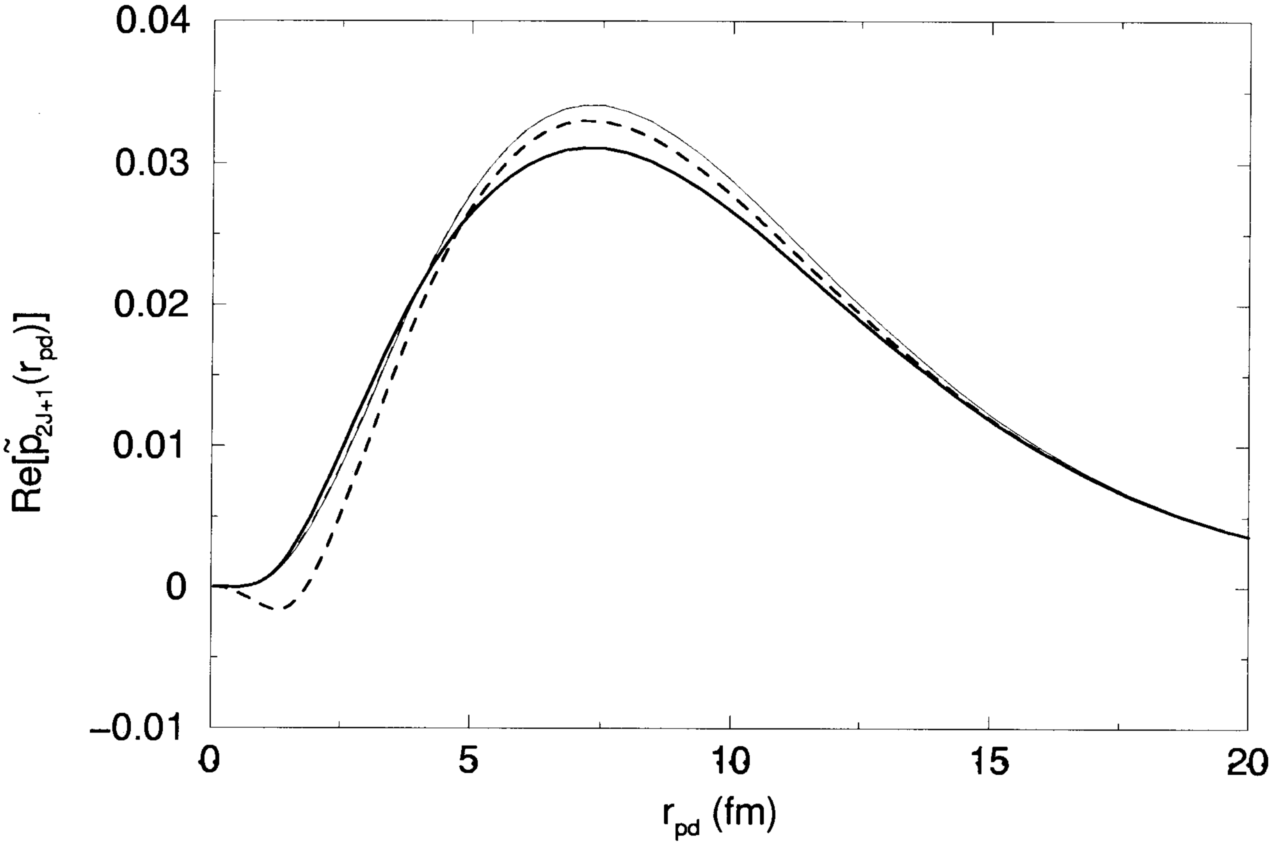
0.04
0.03
0.02
0.01
0
-0.01
0
5
10
15
20
$Re[\tilde{p}_{2J+1}(r_{pd})]$
r_{pd} (fm)

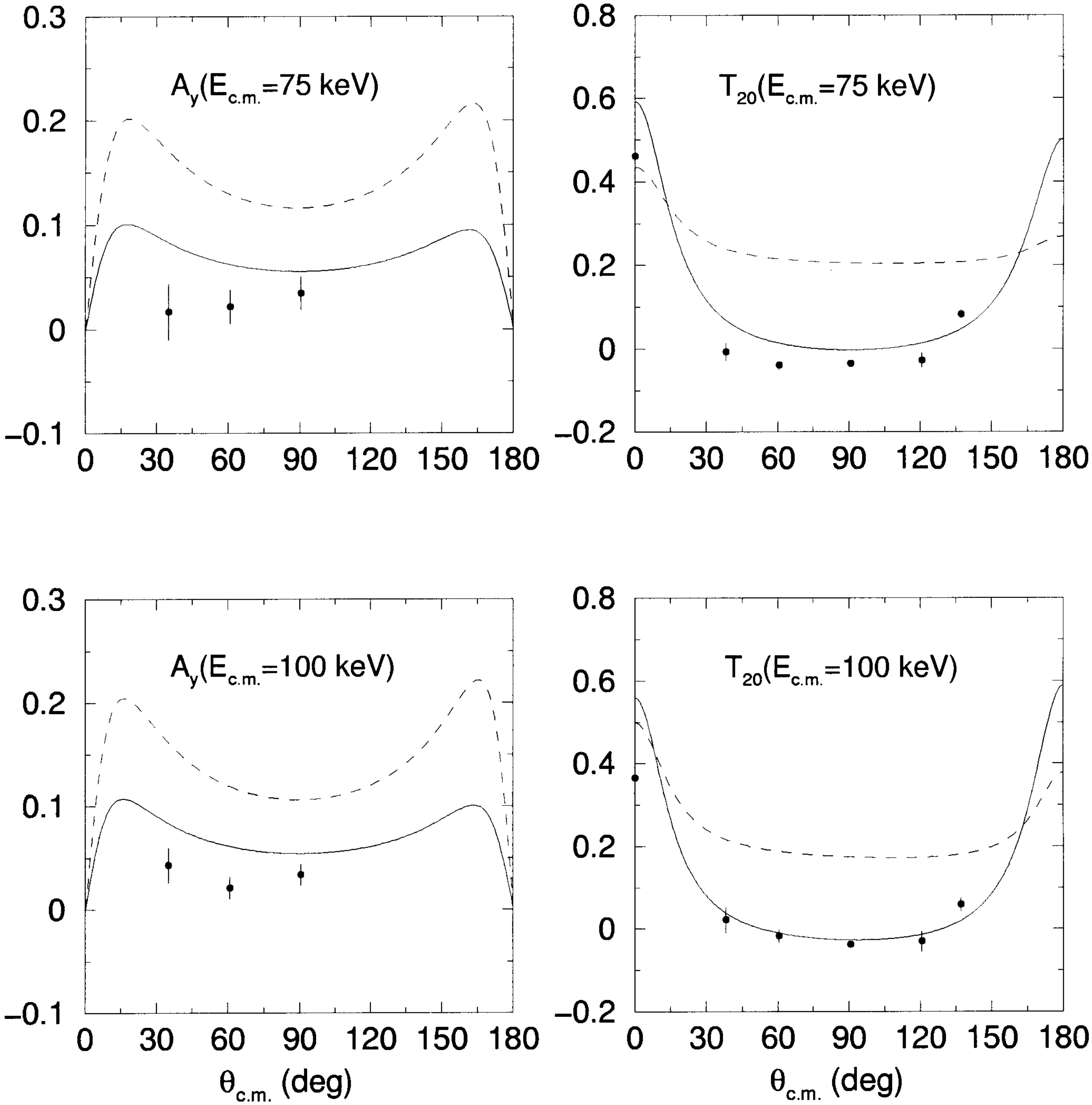

$A_y(E_{c.m.}=75\ keV)$
$T_{20}(E_{c.m.}=75\ keV)$
$A_y(E_{c.m.}=100\ keV)$
$T_{20}(E_{c.m.}=100\ keV)$
0.3
0.2
0.1
0
−0.1
0.8
0.6
0.4
0.2
0
−0.2
0 30 60 90 120 150 180
$\theta_{c.m.}$ (deg)
$\theta_{c.m.}$ (deg)

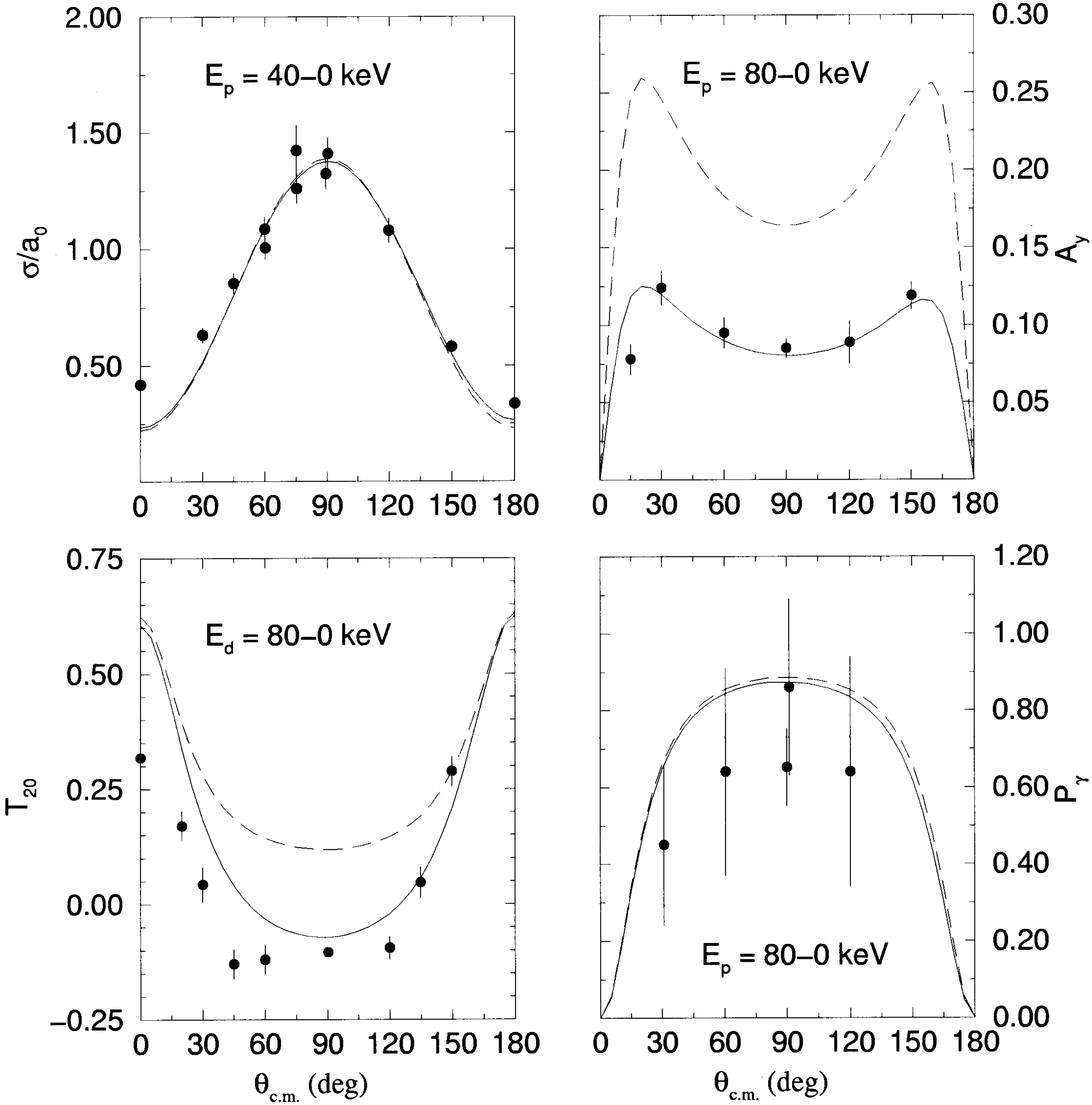

E_p = 40–0 keV
σ/a_0
E_p = 80–0 keV
A_y
E_d = 80–0 keV
T_{20}
E_p = 80–0 keV
P_γ
$\theta_{c.m.}$ (deg)
$\theta_{c.m.}$ (deg)

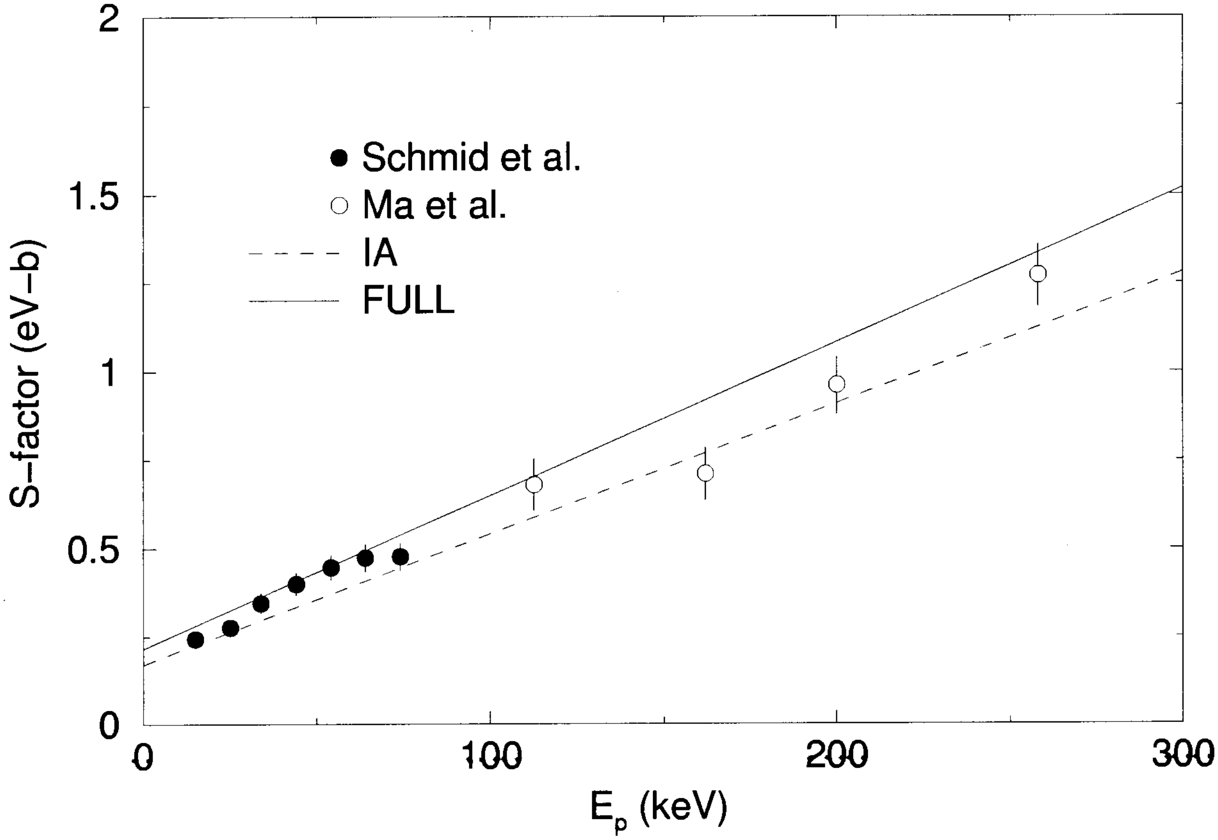

Schmid et al.
Ma et al.
IA
FULL
S–factor (eV–b)
E$_p$ (keV)
0
0.5
1
1.5
2
0
100
200
300

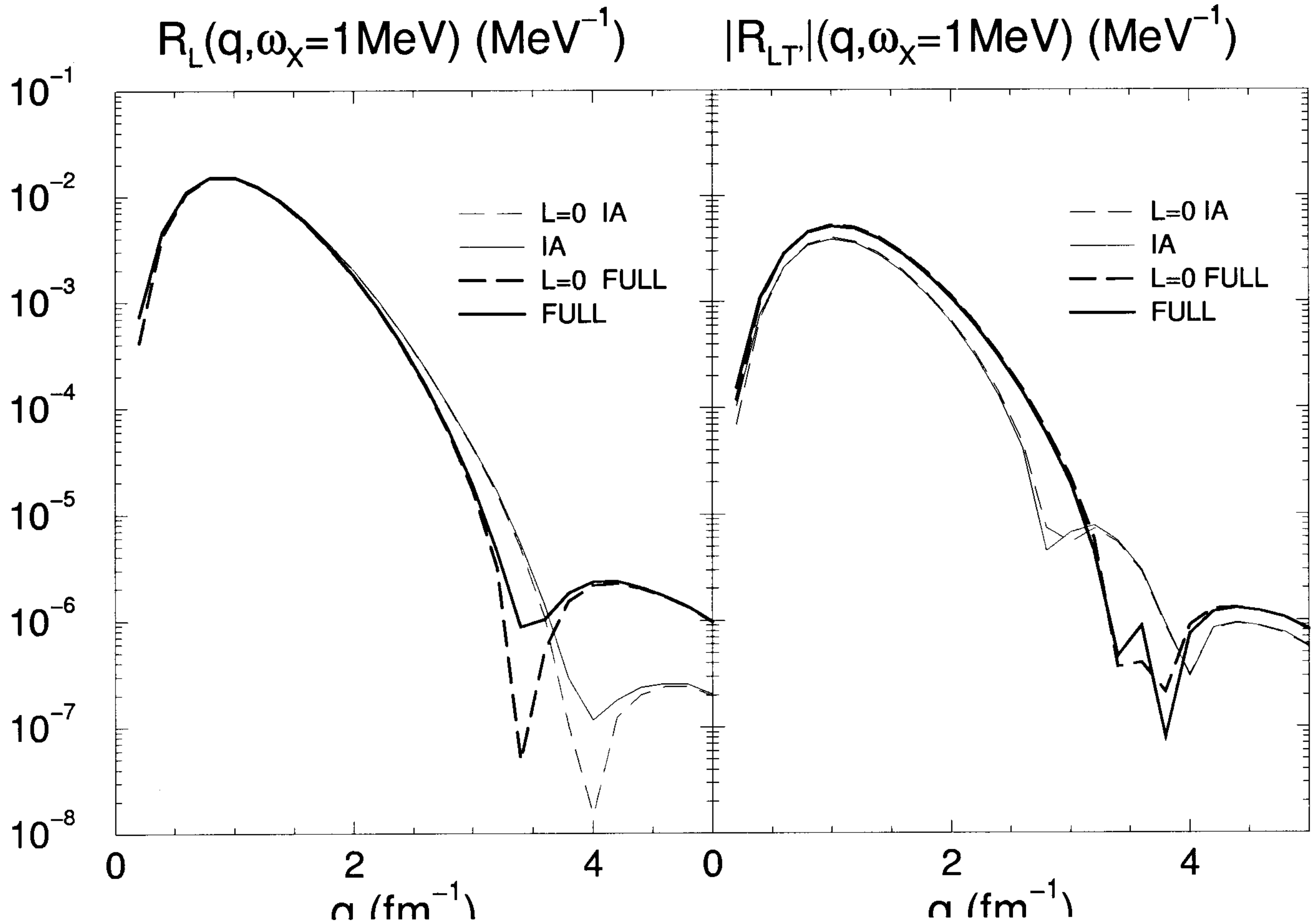

$R_L(q,\omega_X$=1MeV) (MeV^{-1})
$|R_{LT'}|(q,\omega_X$=1MeV) (MeV^{-1})
L=0 IA
IA
L=0 FULL
FULL
L=0 IA
IA
L=0 FULL
FULL
10^{-1}
10^{-2}
10^{-3}
10^{-4}
10^{-5}
10^{-6}
10^{-7}
10^{-8}
0
2
4
0
2
4
q (fm^{-1})
q (fm^{-1})

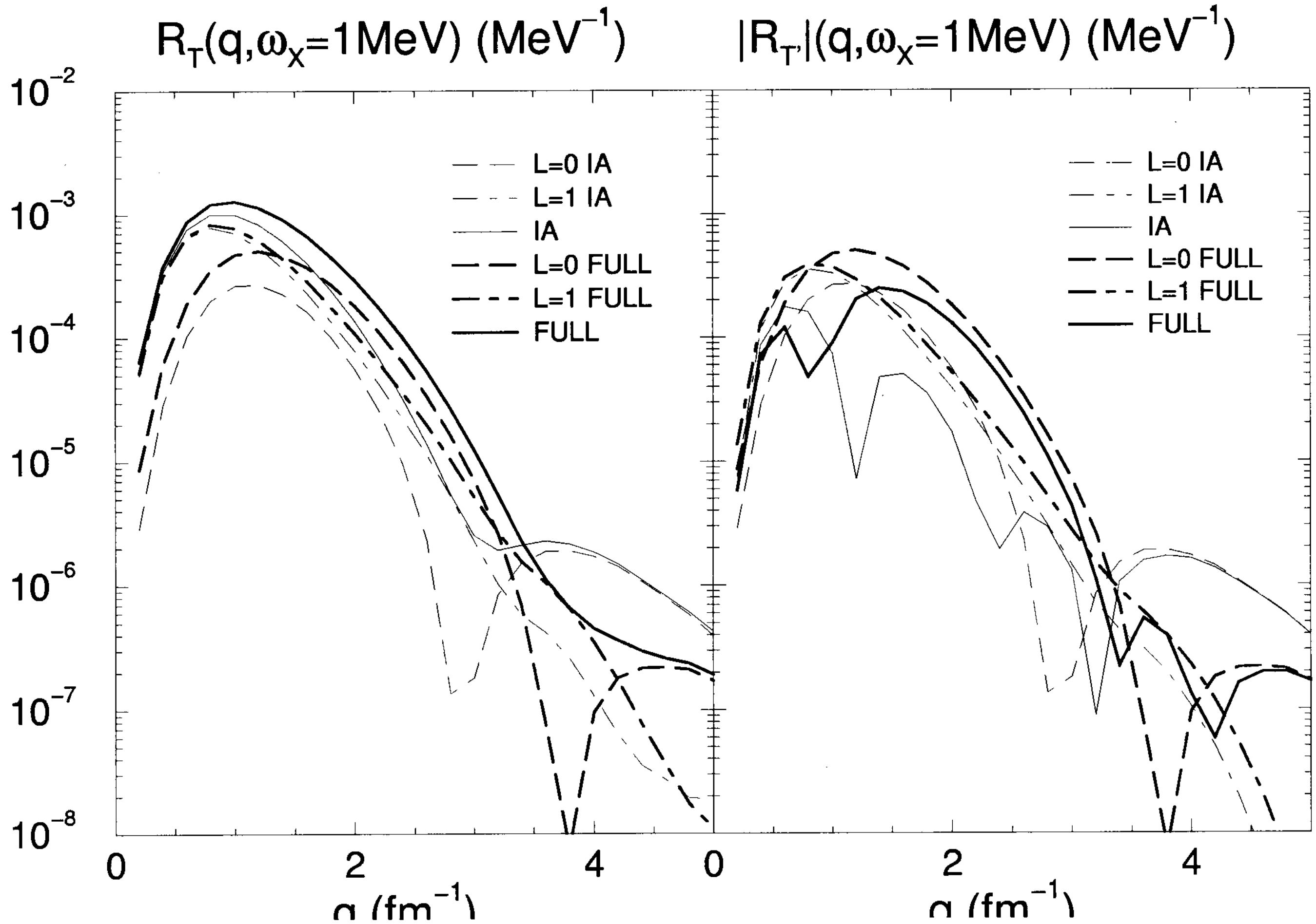

R_T(q,ω_X=1MeV) (MeV^-1)
|R_T'|(q,ω_X=1MeV) (MeV^-1)
L=0 IA
L=1 IA
IA
L=0 FULL
L=1 FULL
FULL
10^-2
10^-3
10^-4
10^-5
10^-6
10^-7
10^-8
0
2
4
q (fm^-1)

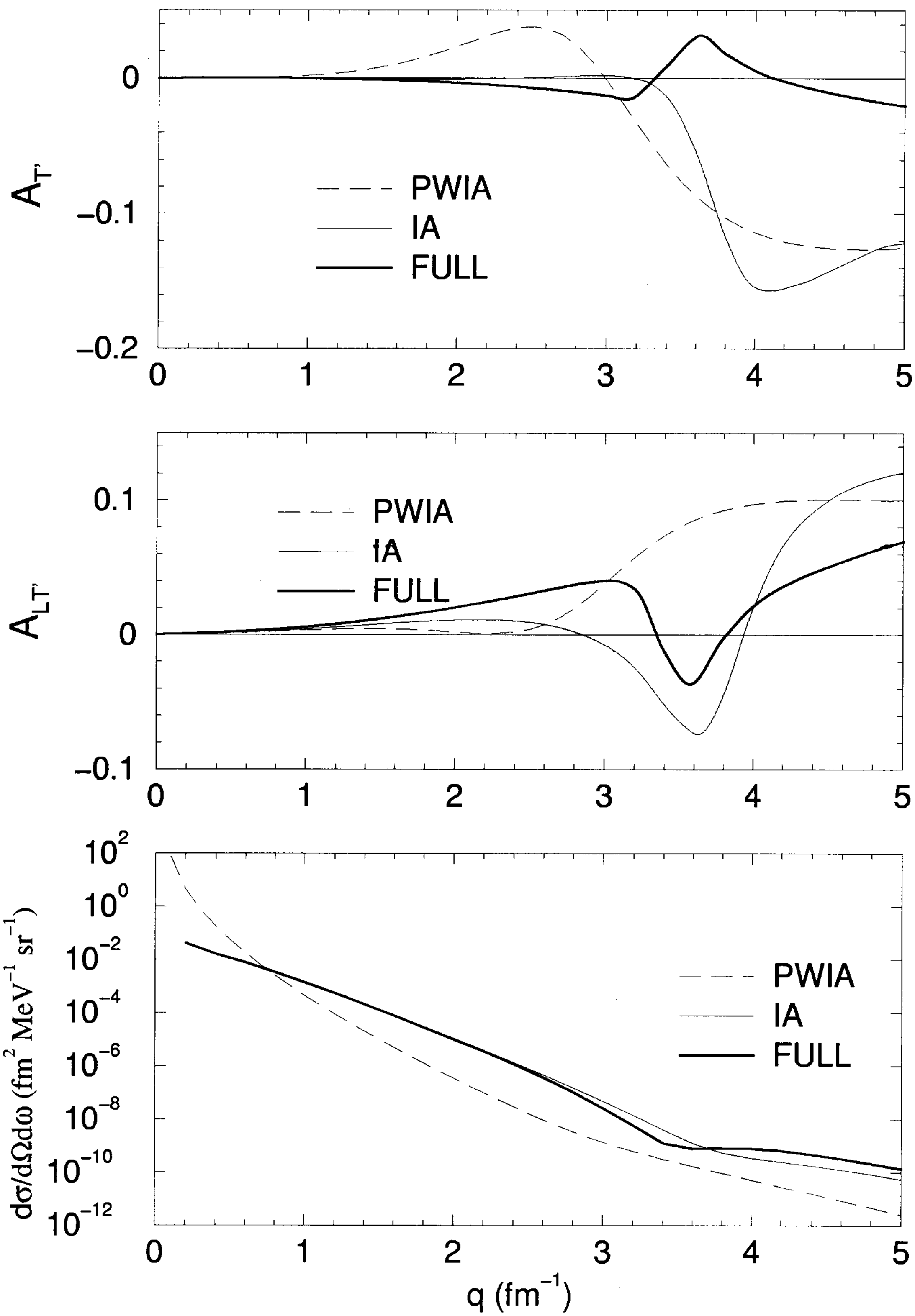

0
−0.1
−0.2
$A_{T'}$
PWIA
IA
FULL
0 1 2 3 4 5
0.1
0
−0.1
$A_{LT'}$
PWIA
IA
FULL
0 1 2 3 4 5
10^{2}
10^{0}
10^{-2}
10^{-4}
10^{-6}
10^{-8}
10^{-10}
10^{-12}
$d\sigma/d\Omega d\omega$ (fm^2 MeV^{-1} sr^{-1})
PWIA
IA
FULL
0 1 2 3 4 5
q (fm^{-1})